

# The GAPS Programme at TNG. TBD: Characterization of the low-density gas giant HAT-P-67 b with GIARPS <sup>★</sup>

D. Sicilia<sup>1</sup>, G. Scandariato<sup>1</sup>, G. Guilluy<sup>2</sup>, M. Esposito<sup>3</sup>, F. Borsa<sup>4</sup>, M. Stangret<sup>5</sup>, C. Di Maio<sup>6</sup>, A. F. Lanza<sup>1</sup>, A. S. Bonomo<sup>2</sup>, S. Desidera<sup>5</sup>, L. Fossati<sup>7</sup>, D. Nardiello<sup>8,5</sup>, A. Sozzetti<sup>2</sup>, L. Malavolta<sup>8</sup>, V. Nascimbeni<sup>5</sup>, M. Rainer<sup>4</sup>, M. C. D'Arpa<sup>6,9</sup>, L. Mancini<sup>10,2,11</sup>, V. Singh<sup>1</sup>, T. Zingales<sup>8</sup>, L. Affer<sup>6</sup>, A. Bignamini<sup>12</sup>, R. Claudi<sup>5</sup>, S. Colombo<sup>6</sup>, R. Cosentino<sup>13</sup>, A. Ghedina<sup>13</sup>, G. Micela<sup>6</sup>, E. Molinari<sup>4</sup>, M. Molinaro<sup>12</sup>, I. Pagano<sup>1</sup>, G. Piotto<sup>8</sup>

<sup>1</sup> INAF - Osservatorio Astrofisico di Catania, Via S. Sofia 78, 95123 Catania, Italy

<sup>2</sup> INAF – Osservatorio Astrofisico di Torino, Via Osservatorio 20, 10025, Pino Torinese, Italy

<sup>3</sup> Thüringer Landessternwarte Tautenburg, Sternwarte 5, 07778 Tautenburg, Germany

<sup>4</sup> INAF – Osservatorio Astronomico di Brera, Via E. Bianchi 46, 23807 Merate, Italy

<sup>5</sup> INAF, Osservatorio Astronomico di Padova, Vicolo dell'Osservatorio 5, Padova I-35122, Italy

<sup>6</sup> INAF – Osservatorio Astronomico di Palermo, Piazza del Parlamento, 1, I-90134 Palermo, Italy

<sup>7</sup> Space Research Institute, Austrian Academy of Sciences, Schmiedl- strasse 6, 8042 Graz, Austria

<sup>8</sup> Dipartimento di Fisica e Astronomia "Galileo Galilei" – Università degli Studi di Padova, Vicolo dell'Osservatorio 3, I-35122 Padova, Italy

<sup>9</sup> University of Palermo, Department of Physics and Chemistry "Emilio Segrè, Via Archirafi 36, Palermo, Italy

<sup>10</sup> Department of Physics, University of Rome "Tor Vergata", Via della Ricerca Scientifica 1, I-00133, Roma, Italy

<sup>11</sup> Max Planck Institute for Astronomy, Königstuhl 17, D-69117, Heidelberg, Germany

<sup>12</sup> INAF – Osservatorio Astronomico di Trieste, via Tiepolo 11, 34143 Trieste, Italy

<sup>13</sup> Fundación Galileo Galilei-INAf, Rambla José Ana Fernández Pérez 7, 38712 Breña Baja, TF, Spain

## ABSTRACT

*Context.* HAT-P-67 b is one of the lowest-density gas giants known to date, making it an excellent target for atmospheric characterization through the transmission spectroscopy technique.

*Aims.* In the framework of the GAPS large programme, we collected four transit events of HAT-P-67 b with the aim of studying the exoplanet atmosphere and deriving the orbital projected obliquity.

*Methods.* We exploited the high-precision GIARPS (GIANO-B + HARPS-N) observing mode of the Telescopio Nazionale Galileo (TNG), along with additional archival TESS photometry, to explore the activity level of the host star. We performed transmission spectroscopy, both in the visible (VIS) and in the near-infrared (nIR) wavelength range, and analysed the Rossiter–McLaughlin (RML) effect both fitting the radial velocities and the Doppler shadow. Based on the TESS photometry, we redetermined the transit parameters of HAT-P-67 b.

*Results.* By modelling the RML effect, we derived a sky-projected obliquity of  $(2.2 \pm 0.4)^\circ$  indicating an aligned planetary orbit. The chromospheric activity index  $\log R'_{\text{HK}}$ , the CCF profile, and the variability in the transmission spectrum of the  $H\alpha$  line suggest that the host star shows signatures of stellar activity and/or pulsations. We found no evidence of atomic or molecular species in the optical transmission spectra, with the exception of pseudo-signals corresponding to Cr I, Fe I,  $H\alpha$ , Na I, and Ti I. In the nIR range, we found an absorption signal of the He I triplet of  $5.56^{+0.29}_{-0.30}\%$  ( $19.0\sigma$ ), corresponding to an effective planetary radius of  $\sim 3 R_p$  (where  $R_p \sim 2 R_J$ ) which extends beyond the planet's Roche Lobe radius.

*Conclusions.* Owing to the stellar variability, together with the high uncertainty of the model, we could not confirm the planetary origin of the signals found in the optical transmission spectrum. On the other hand, we confirmed previous detections of the infrared He I triplet, providing a  $19.0\sigma$  detection. Our finding indicates that the planet's atmosphere is evaporating.

**Key words.** planetary systems - planets and satellites: atmospheres - techniques: photometric - techniques: spectroscopic - planets and satellites: individual (HAT-P-67 b)

## 1. Introduction

Over the last few decades, the field of exoplanet research has grown rapidly, revealing that extrasolar systems are very common and extremely diverse in masses, radii, temperatures, and orbital parameters. Thanks to increasingly efficient ground- and

space-based surveys, today we are able to explore the exoplanet compositions and atmospheres in an ever larger sample.

Puffy planets (i.e., planets with large radii and very low densities) constitute some of the most favorable targets for characterization through the transmission spectroscopy technique (e.g., Sedaghati et al. 2016; Allart et al. 2020; Colón et al. 2020; Czesla et al. 2022). Due to their large radius and low surface gravity, they are expected to present a high atmospheric pressure scale height ( $H$ ), which is the characteristic length scale of the atmosphere. The amplitude of an absorption signal in transmission spectroscopy, i.e. the change in measured transit depth, is pro-

<sup>★</sup> Based on observations made with the Italian *Telescopio Nazionale Galileo* (TNG) operated on the island of La Palma by the *Fundación Galileo Galilei* (FGG) of the *Istituto Nazionale di Astrofisica* (INAF) at the Spanish *Observatorio del Roque de los Muchachos* of the *Instituto de Astrofísica de Canarias*.

Table 1: Summary of TESS and GIARPS data used in this work.

TESS						
Sector	Date start [UTC]	Date end [UTC]	$N_{\text{transits}}$	$t_{\text{exp}}[\text{s}]$	Simultaneous spectroscopy	
24	2020-04-16 06:55:19	2020-05-12 18:41:18	6	120	No	
26	2020-06-09 18:15:17	2020-07-04 15:11:16	6	120	Yes (N2)	
51	2022-04-23 10:34:51	2022-05-18 00:46:50	3	120	No	
52	2022-05-19 03:04:50	2022-06-12 13:46:49	5	120	No	
53	2022-06-13 11:44:48	2022-07-08 11:26:47	4	120	No	

GIARPS							
Night	$N_{\text{obs}}^a$	$t_{\text{exp}}[\text{s}]$	$N_{\text{obs}}^a$	$t_{\text{exp}}[\text{s}]$	Airmass <sup>b</sup>	S/N (min-max) <sup>c</sup>	Seeing
	HARPS-N		GIANO-B				
N1: 2020-05-26	45 (42)	600	80 (71)	300	1.69-1.04-1.34	42.6-67.1	1.0"
N2: 2020-06-24	31 (23)	600	50 (39)	300	1.18-1.04-1.27	29.8-52.0	1-3" very variable
N3: 2021-06-10	45 (40)	600	-	-	1.47-1.04-1.56	22.2-47.0	0.9"
N4: 2023-07-10	42 (37)	600	68 (59)	300	1.14-1.04-2.08	23.0-36.3	0.7"

<sup>a</sup> In parenthesis: the number of analysed spectra that are considered in-transit (between the first and fourth contact).

<sup>b</sup> The values are extracted from the FITS header of the HARPS-N spectra, and indicate the airmass at the beginning, during its minimum, and at the end of the transit.

<sup>c</sup> The signal-to-noise ratio (S/N) indicated is extracted from the FITS header of the HARPS-N spectra on the 53rd order that contains the sodium feature. The values are more or less the same as those of the GIANO-B spectra extracted in the region of the He I triplet.

portional to  $H$  ( $2HR_p/R_\star^2$ , Brown 2001). Transmission spectral signals are typically on the order of 1 to  $\sim 5H$  in size, thus if the transit depth can be measured to about  $1H$  in precision with sufficient spectral resolution, detectable spectral features would begin to appear. Since puffy planets are characterized by atmospheres with higher  $H$  values, they are expected to present stronger absorption signals (assuming the host star's brightness and the signal-to-noise ratio high enough). Some of them that have been explored so far, such as KELT-11 b (Pepper et al. 2017), WASP-17 b (Anderson et al. 2010), and WASP-127 b (Lam et al. 2017), show even  $H \gtrsim 1900$  km (compared to  $\sim 10$  km on Earth, or  $\sim 27$  km on Jupiter). In these cases, the signal in transmission for  $1H$  is of the order of  $10^{-2} - 1\%$ , (compared to  $\sim 2 \cdot 10^{-5}\%$  on Earth, and  $\sim 10^{-3}\%$  on Jupiter).

HAT-P-67 b (Zhou et al. 2017) is a gas giant puffy planet transiting a rapidly rotating ( $v \sin i = 35.8 \pm 1.1 \text{ km s}^{-1}$ ) F-subgiant star every  $\sim 4.8$  days, at the orbital distance of 0.065 au. It is one of the largest ( $R_p \sim 2 R_J$ ) and lowest density ( $\rho \sim 0.05 \text{ g cm}^{-3}$ ) planets found to date. Due to the rapid rotation of the host star, the radial velocity (RV) technique does not allow to precisely determine the semi-amplitude of the planet  $K_p$  and, consequently, the mass of the planet, for which there is only an upper limit ( $M_p < 0.59 M_J$ ). A lower limit ( $M_p > 0.056 M_J$ ) was also applied by Zhou et al. (2017) when assuming the planet is not undergoing Roche lobe overflow. The host star belongs to a binary stellar system; however, the M dwarf companion (HAT-P-67B, Mugrauer 2019), has a projected separation of about 3400 au, thus not being a source of contamination for observations.

The low density and high irradiation of HAT-P-67 b (it receives approximately two times the incident flux of a zero-age main-sequence star) also results in a bloated atmosphere with a large  $H$  of  $\sim 3500$  km (assuming an  $\text{H}_2/\text{He}$  mixture of near-solar composition atmosphere). This makes the planet another good candidate for transmission spectroscopy studies.

Recently, the atmosphere of HAT-P-67 b was explored by Bello-Arufe et al. (2023), through the analysis of one full tran-

sit acquired with CARMENES (Quirrenbach et al. 2016). The authors reported the detection of Ca II and Na I (with a statistical significance of  $13.2\sigma$  and  $4.6\sigma$  respectively), which they ascribe to the planetary signal. Besides, they found strong variability in the  $\text{H}\alpha$  line and in the He triplet, suggesting the possible presence of an extended planetary outflow. This extended atmosphere was confirmed by Gully-Santiago et al. (2023) who reported an absorption depth up to 10% in the stellar He I triplet, thanks to a series of observations taken with the Habitable Zone Planet Finder Spectrograph (HPF, Mahadevan et al. 2012). Besides, Gully-Santiago et al. (2023) derived an increase of the stellar radius ( $2.65 \pm 0.12 R_J$ ), to match the updated Gaia DR3 distance (8.7 % farther than previously estimated by Zhou et al. 2017). However, this update does not entail any major changes to the rest of the parameters derived by Zhou et al. (2017).

HAT-P-67 b is one of the targets of the atmospheric sample of the Global Architecture of Planetary Systems (GAPS) (Gulluy et al. 2022). Thanks to the availability of the HARPS-N spectrograph (Cosentino et al. 2012), mounted at the Italian Telescopio Nazionale Galileo (TNG) in La Palma, we have collected and analysed four transits of HAT-P-67 b. The GIARPS observing mode (Claudi et al. 2018), allowed us to gather simultaneous observations both in the visible (VIS) with HARPS-N (0.39 - 0.68  $\mu\text{m}$ ,  $R \simeq 115,000$ ), and in the near infrared (nIR) with GIANO-B (0.95 - 2.45  $\mu\text{m}$ ,  $R \simeq 50,000$ ). Thereby providing capability to investigate the system architecture and the exoplanet atmosphere in a wider wavelength range.

A description of the observations used in this work is presented in Sect. 2. Taking advantage of multiple Transiting Exoplanet Survey Satellite (TESS, Ricker et al. 2014) light curves, and high precision HARPS-N RV time series, we redetermined the orbital parameters and analysed the RML effect, in Sect. 3. We also tried to explore the activity level of the host star using different indicators in Sect. 4. We presented the characterization of the planetary atmosphere through the analysis of the transmis-



Table 2: Adopted stellar parameters. All parameters listed here are taken from Zhou et al. (2017), except the stellar radius which is taken from Gully-Santiago et al. (2023).

Symbol	Value
$T_{\text{eff}}$ [K]	$6406^{+65}_{-61}$
[Fe/H]	$-0.080 \pm 0.050$
$v \sin i$ [km s $^{-1}$ ]	$35.8 \pm 1.1$
$M_{\star}$ [ $M_{\odot}$ ]	$1.642^{+0.155}_{-0.072}$
$R_{\star}$ [ $R_{\odot}$ ]	$2.65 \pm 0.12$
$\log g_{\star}$ [ $\log_{10}(\text{cm s}^{-2})$ ]	$3.854^{+0.014}_{-0.023}$

sion spectrum both in the VIS and in the nIR in Sect. 5. Finally, we discussed our findings in Sect. 6.

## 2. Observations

For the analysis of the HAT-P-67 system we used both high-resolution VIS and nIR spectroscopy with the GIARPS (GIANO-B + HARPS-N) observing mode of the TNG, as well as photometry from TESS. A summary of the observations and stellar parameters adopted in this work for analysis is reported in Tables 1 and 2, respectively.

### 2.1. Spectroscopy

We observed four transits of HAT-P-67 b, three of which in the GIARPS mode, in the framework of the GAPS large/long-term program (Covino et al. 2013).

The exposure time ( $t_{\text{exp}}$ ) of the observations of HAT-P-67 b was fixed to 600 s for HARPS-N, and 300 s for GIANO-B, yielding runs of 46, 31, 46 and 42 VIS spectra, and 80, 50 and 68 nIR spectra during each transit. However, the very long duration of the transit ( $\sim 7$  hours) results in quite a low number of out-of-transit spectra with respect to the total acquired spectra (only 23 out of 165 in the VIS, and 29 of 198 in the nIR). To determine whether a spectrum was (fully)in-transit or out-of-transit, we considered the half of  $t_{\text{exp}}$  in addition to the BJD (Barycentric Julian Date) of the observation. Sky spectra were retrieved simultaneously with the science observations thanks to a dedicated fiber, named fiber B, pointing at a fixed position at around 10 arcsec from the target star, ensuring the same atmospheric conditions in both spectra.

In the first run (N1), there are hints of stellar activity which we discussed in Section 4; the second run (N2) covers only the second half of the transit and is characterized by a strong variability in seeing (1 - 3 arcsec), but it is the run with the highest number of out-of-transit spectra; during the third run (N3), GIANO-B was offline so we collected only HARPS-N observations which present some spectra with a lower signal-to-noise-ratio (S/N), probably due to thin clouds and the presence of some calima; the fourth run (N4) does not cover the egress and the post-transit phase and is characterized by a lower S/N compared to the other nights (see Fig. A.1, right panel). We decided to remove the first exposure of N1 since the corresponding RV measurement deviates from the expected pattern, creating a distortion of the fit. For transmission spectrum analysis only, we also discarded the exposure with the lowest S/N of N3 ( $< 20$ , at the center of the 53rd order, with the sodium doublet).

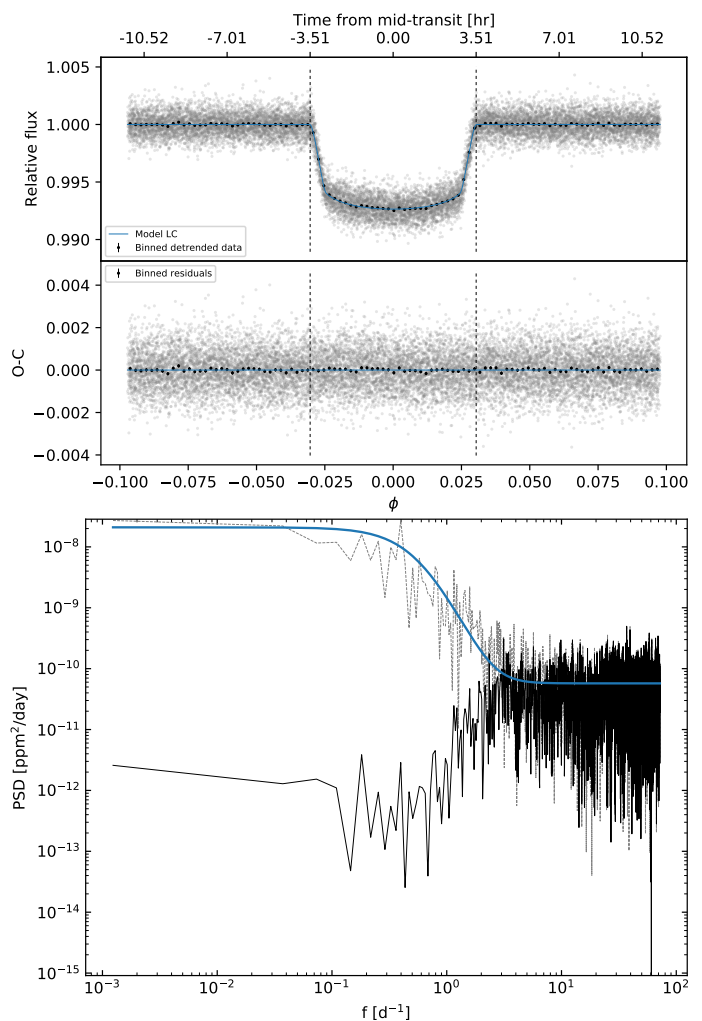


Fig. 1: Results of the fit of the transit light curves (LCs). *Top* - Phase-folding of the detrended data (*top panel*) and the corresponding O-C diagram (*bottom panel*). For clarity, in each panel, we show the binned data with black dots. *Bottom* - The gray dashed line shows the power spectral density (PSD) of the data after removing the best-fit transit model, while the blue solid line represents the combined PSD of the best-fit Gaussian process (GP) (the shoulder at  $f \lesssim 1 \text{ d}^{-1}$ ) and the white noise in the data (the plateau at  $f \gtrsim 10 \text{ d}^{-1}$ ). The black line is the PSD of the residuals of the best fit, showing that the power excess at low frequencies has been effectively removed by the GP in the model.

### 2.2. Photometry

The time span covered by our spectroscopic survey almost completely overlaps with the TESS (Ricker et al. 2014) observations of HAT-P-67. This allowed us to determine the precise ephemeris of HAT-P-67 b and closest to the epochs of our GIARPS data, thus best suited for the extraction of the transmission signal of HAT-P-67 b. TESS observed the HAT-P-67 system with a 2 min cadence in sector 24 (S24, from 2020 April 16 to 2020 May 12, six transits observed), sector 26 (S26, from 2020 June 9 to 2020 July 4, six transits), sector 51 (S51, from 2022 April 23 to 2022 May 18, three transits), sector 52 (S52, from 2022 May 19 to 2022 June 12, five transits), and sector 53 (S53, from 2022 June 13 to 2022 July 8, four transits). Of the analysed TESS sectors, only S26 covers one of the simultaneously observed tran-

Table 3: Model parameters for the fit of the TESS data.

Free parameters	Symbol	Units	C.I. <sup>a</sup>	Prior
GP amplitude	$\log h$	—	-7.49(7)	$U(-8,-5)$
GP timescale	$\log \frac{\lambda}{1 \text{ day}}$	—	-0.76(9)	$U(-4,2)$
Time of transit	$T_0$	BJD <sub>TDB</sub>	2459338.0790(1)	$U(2459338.078,2459338.080)$
Orbital frequency	$\nu_{\text{orb}}$	d <sup>-1</sup>	0.20789543(7)	$U(0.207895,0.207897)$
Stellar density	$\rho_{\star}$	$\rho_{\odot}$	0.083(2)	$U(0.07,0.09)$
Radii ratio	$R_p/R_{\star}$	—	0.0821(2)	$U(0.075,0.090)$
Impact parameter	$b$	—	0.44(2)	$U(0.3,0.5)$
First LD coef.	$q_1$	—	0.16(2)	$U(0,1)$
Second LD coef.	$q_2$	—	0.33(8)	$U(0,1)$
Derived parameters	Symbol	Units	C.I.	
Planetary radius	$R_p$	$R_J$	2.1(1)	including the stellar radius uncertainty
Orbital period	$P_{\text{orb}}$	d	4.810110(2)	
Total transit duration	$T_{14}$	hr	7.01(1)	
Full transit duration	$T_{23}$	hr	5.70(2)	
Scaled semi-major axis	$a/R_{\star}$	—	5.22(4)	
Orbital inclination	$i$	deg	85.1(2)	

Notes. <sup>(a)</sup> The 68% confidence interval. Uncertainties expressed in parentheses refer to the last digit.

sits with GIARPS which corresponds to the half-transit retrieved during the second night.

Using the package `lightkurve` (Lightkurve Collaboration et al. 2018), we retrieved the Pre-search Data Conditioning Single Aperture Photometry (PDCSAP), which is corrected for instrumental systematics and for contamination from some nearby stars (Smith et al. 2012; Stumpe et al. 2012, 2014). We took into consideration only the photometry with good quality flag.

### 3. Orbital parameters

We redetermined the HAT-P-67 b transit parameters. Given the difficulty in the interpretation of the long-term stellar variability (Sect. 4), we trimmed segments of the LCs centered on the transit events and as wide as three times the expected transit duration. Each photometric segment was normalised to the median out-of-transit flux. A total of 22 transits were extracted from the TESS LCs.

We adopted the same Bayesian approach described in Scandariato et al. (2022): we maximized the likelihood of a model that includes the combined transit fit along with a GP to detrend against long-term stellar/instrumental systematics. The presence of long-term trends is testified by the PSD of the data, that monotonically increases with decreasing frequency. We thus used a Matérn 3/2 kernel for the GP (see Fig. 1), being it characterized by a PSD similar to the data. This approach is less time-consuming than fitting for each transit a polynomial trend. Moreover, it greatly reduces the dimensionality of the model: 2 free parameters of the GP model against  $22 \times (deg + 1)$  parameters for the polynomial detrending, where  $deg$  is the polynomial degree used for the detrending.

The transit profile was computed using the quadratic limb darkening (LD) law of Mandel & Agol (2002) with the reparametrization of the LD coefficients of Kipping (2013). We also included in the model a re-normalisation factor and a jitter term to fit the white noise not included in the nominal photometric uncertainties. We sampled the parameter space in a Markov Chain Monte Carlo (MCMC) framework using the Python `emcee` package version 3.1.3 (Foreman-Mackey et al. 2013). We used 44 walkers, corresponding to four times the

number of free parameters. We ran the chains for 50 000 samplings, enough to ensure convergence following the criterion described in Goodman & Weare (2010). We used flat priors (listed in Table 3) for all the fitting parameters. We ran the code in the HOTCAT computing infrastructure (Bertocco et al. 2020; Taffoni et al. 2020). The results of the MCMC fit are listed in Table 3. The best-fitting model is over-plotted to the phase-folded data in Fig. 1.

Then, we used the RV time series to detect the RML effect (see e.g., Albrecht et al. 2022) and measure the sky-projected angle between the stellar spin axis and the planet orbital axis. The data were reduced using the 3.7 version of the HARPS-N Data Reduction Software (DRS) through the Yabi web application, hosted at the Italian center for Astronomical Archive (IA2)<sup>1</sup>. The RV measurements were obtained using a G2 mask template and a cross-correlation function (CCF) width of 250 km s<sup>-1</sup>, with a step of 0.25 km s<sup>-1</sup>. The lists of the RVs are presented in Tables A.1-A.4, together with the stellar activity index  $\log R'_{\text{HK}}$  (see Sect. 4). We did not consider the observations taken on N2 as they do not cover a full transit and were affected by highly variable seeing (see Table 1 and Fig. A.1). The RML effect modelling and the RV fitting were carried out using a code developed by us within the MATLAB software environment. A detailed explanation of the working principles of the code can be found in Esposito et al. (2017).

For the fit of the RML effect, most of the relevant parameters were adopted from the literature ( $M_{\star}$ ,  $R_{\star}$ ,  $\nu \sin i$ , see Table 2) and from our analysis of the TESS LCs ( $T_0$ ,  $P_{\text{orb}}$ ,  $i$ ,  $R_p$ , see Table 3). The only parameters which were left free to vary were the barycentric RV ( $\nu_{\text{sys}}$ ) and the projected spin-orbit angle ( $\lambda$ ). Given the large uncertainty on the planet's mass and considering that significant RV variations induced by stellar activity are expected on a time scale of a few hours, we also added as a free parameter an RV linear trend (LT).

We fitted separately the three transit RV time series taken on 2020-05-26, 2021-06-10 and 2023-07-10. For the first (second, third) transit the best-fit results are:  $\lambda = 6.4 \pm 7.5 \text{ deg}$  ( $8 \pm 11 \text{ deg}$ ,  $10 \pm 12 \text{ deg}$ ),  $\nu_{\text{sys}} = -1968 \pm 22 \text{ m s}^{-1}$  ( $-2225 \pm 33 \text{ m s}^{-1}$ ,  $-2250$

<sup>1</sup> <https://www.ia2.inaf.it>

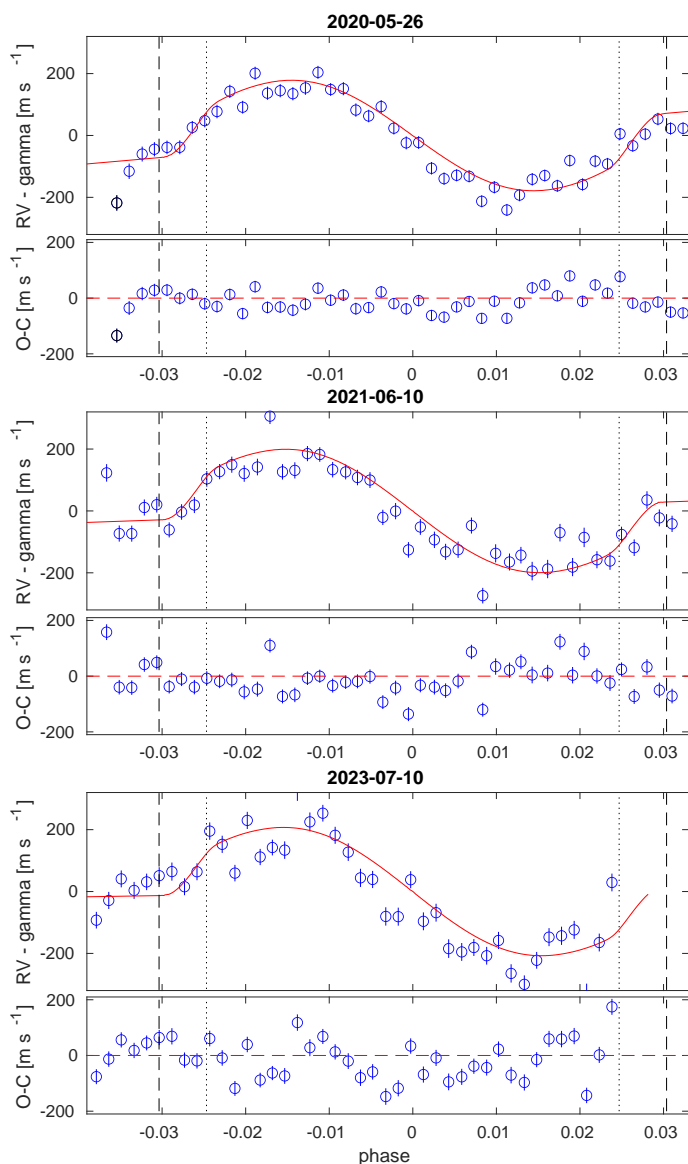


Fig. 2: The Rossiter-McLaughlin effect analysis. *Top* - RV time series taken during the transit on 2020-05-26 (N1). The best-fit model is superimposed and the corresponding residuals are shown in the lower panel. The dashed black lines indicate the points of first and fourth contact of the transit, while the dotted black lines represent the points of second and third contact. *Middle* - The same for the transit on 2021-06-10 (N3). *Bottom* - The same for the transit on 2023-07-10 (N4).

$\pm 45 \text{ m s}^{-1}$ ) and  $LT = 0.0057 \pm 0.0015 \text{ m s}^{-2}$  ( $0.0021 \pm 0.0020 \text{ m s}^{-2}$ ,  $0.0010 \pm 0.0020 \text{ m s}^{-2}$ ). The measure of  $v_{\text{sys}}$  found for N1 is statistically far from the values found for the other nights; this offset is likely due to a higher stellar variability (see Sect. 4). The three RV time series with the best-fit models superimposed are shown in Fig. 2.

In order to improve the precision on  $\lambda$ , we then performed a fit to the Doppler shadow, in the same way as in Borsa et al. (2021b). Indeed, for relatively fast rotators, such as HAT-P-67, the tomography method can better constrain  $\lambda$  than RVs. The Doppler shadow model was taken from EXOFASTv2 (Eastman 2017), and fitted to the data in a Bayesian framework by employing a Differential Evolution Markov chain Monte Carlo (DE-MCMC) technique (Ter Braak 2006; Eastman et al. 2013), run-

ning ten DE-MCMC chains of 50,000 steps and discarding the burn-in, until convergence was reached. We fixed  $T_0$  and  $P_{\text{orb}}$  as in Table 3, as well as the quadratic limb darkening parameters ( $\mu_1 = 0.43$  and  $\mu_2 = 0.25$ , taken from ExoCTK<sup>2</sup>) and  $v_{\text{sys}} = -2000 \text{ m s}^{-1}$ . We note that the  $v_{\text{sys}}$  value cannot be well constrained by the Doppler tomography fit for fast rotators, on the contrary of what happens for RVs, and that changing this value within the differences found by the RVs analysis of the different transits does not affect the results. We left  $i$ ,  $a/R_*$ ,  $R_p/R_*$  as free parameters with values and error-bars in Table 3 as priors. The  $v \sin i$  (which includes macroturbulence) and  $\lambda$  parameters were left free with uniform priors. The medians and the 15.86% and 84.14% quantiles of the posterior distributions were taken as the best values and  $1\sigma$  uncertainties. We fitted independently all the four transits, finding  $v \sin i = 39.2 \pm 0.5$ ,  $36.7 \pm 0.9$ ,  $38.3 \pm 0.7$ ,  $39.5 \pm 0.8 \text{ km s}^{-1}$  and  $\lambda = 1.0 \pm 0.6$ ,  $5.5 \pm 1.1$ ,  $1.2 \pm 0.8$ ,  $3.2 \pm 0.9$  degrees for night 1 to 4, respectively. When fitting the four transits together, we find  $v \sin i = 39.3 \pm 0.4 \text{ km s}^{-1}$  and  $\lambda = 2.2 \pm 0.4$  degrees. As expected, the best values of  $\lambda$  are both more accurate and precise than the ones found by fitting the RVs. We note that the  $v \sin i$  value is compatible with that found by Zhou et al. (2017) within  $3\sigma$ .

#### 4. Stellar activity

Stellar activity can mimic spurious features in the retrieved transmission spectra (e.g., Oshagh et al. 2014; Apai et al. 2018). To detect potential stellar effects in the analysed nights, we first measured the  $\log R'_{\text{HK}}$  chromospheric activity index (Fig. 3 and Tables A.1-A.4). We extracted it from the HARPS-N spectra through the YABI platform (Hunter et al. 2012), using a  $B-V$  color index of 0.441 mag. We derived average values of  $-4.651 \pm 0.001$ ,  $-4.675 \pm 0.003$ ,  $-4.743 \pm 0.004$ , and  $-4.704 \pm 0.007$  for N1, N2, N3 and N4 respectively. The obtained values are moderately larger than the solar value at the maximum of activity ( $-4.75$  according to Dumusque et al. 2011; or  $-4.905$  according to Egeland et al. 2017). N1 presents slightly higher activity compared with the other nights, while N4 is characterized by greater uncertainty, likely due to the highest S/N and airmass (Fig. A.1). However, it is important to note that the chromospheric  $\log R'_{\text{HK}}$  index is thought to be significantly depressed in stars with transiting giant planets. This is because of the absorption by a circumstellar torus produced by planetary evaporation that is particularly strong in planets with a very low surface gravity, such as HAT-P-67 b. Considering the data and the linear models relating the chromospheric index with the inverse of the surface gravity (Lanza 2014; Fossati et al. 2015), the true value of  $\log R'_{\text{HK}}$  of HAT-P-67 could be larger by at least 0.4-0.5, that is, it can approach  $-4.2$ .

The occurrence of phenomena associated with stellar activity during N1 is also reflected in the corresponding CCFs linear profile (Fig. 4, left panels), which is much more distorted and time-varying compared with N3 and N4 (N2 is not considered here since it covers only half transit). The distortion of the stellar CCF also strongly affects the measured RVs. Indeed, the systemic velocity obtained fitting the RVs on N1 presents an offset of  $\sim 200 \text{ m/s}$  compared to N3 and N4 (see Sect. 3).

Most likely, the origin of this distortion is some kind of stellar variability. To support this hypothesis, for each night we Doppler-shifted the individual CCFs to the stellar rest frame and computed the average CCF. Then we divided each CCF by the average one and built the 2-dimensional stack of the residuals,

<sup>2</sup> [https://exoctk.stsci.edu/limb\\_darkening](https://exoctk.stsci.edu/limb_darkening)



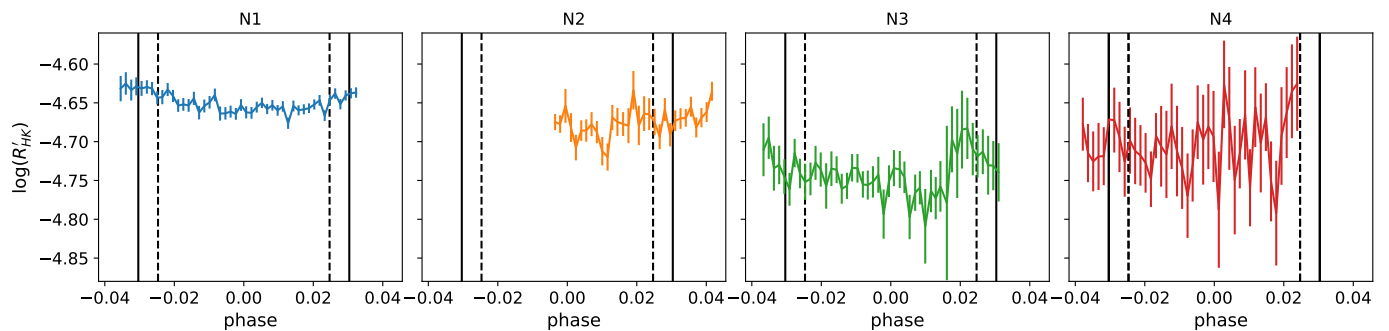


Fig. 3: The activity indicator  $\log R'_{\text{HK}}$  as a function of the time for each night. The continuous black lines indicate the points of first and fourth contact of the transit, while the dashed black lines represent the points of second and third contact.

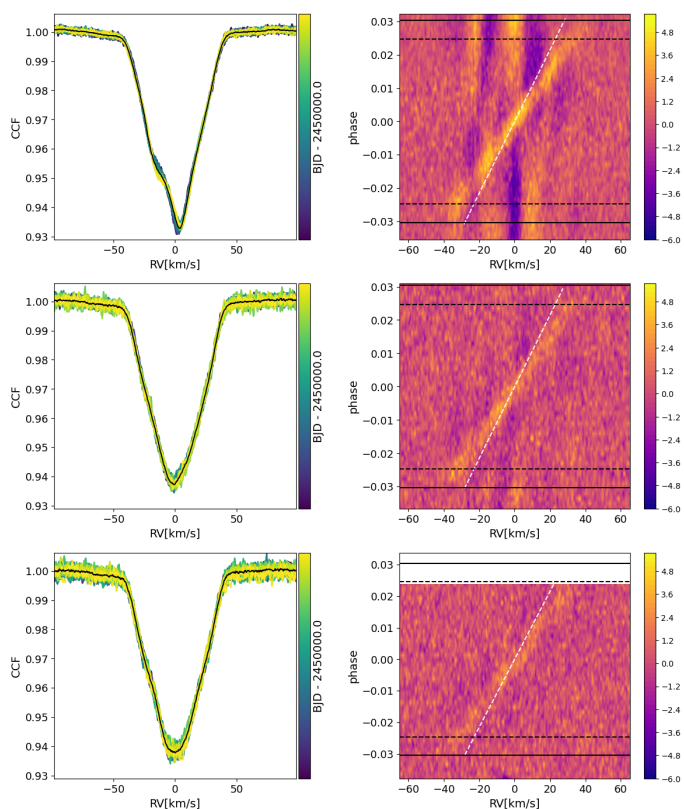


Fig. 4: CCFs for N1 (first row), N3 (second row), N4 (third row) extracted from the DRS using a G2 mask. *Left*: CCFs linear profiles as a function of time; the black line indicates the average CCF. *Right*: two-dimensional maps of the CCFs as a function of orbital phase and RV in the stellar rest frame; the four horizontal black lines show the times of transit contacts. The straight white line shows the expected planetary keplerian velocity  $K_p$  using a planetary mass value of  $\sim 0.34 M_J$  (Zhou et al. 2017).

shown in the right panels of Fig. 4. In addition to the evident Doppler shadow due to the planetary transit (the tilted trace), some evident vertical patterns can be seen in N1, even outside the transit. Being at rest in the stellar rest frame, these patterns can not be ascribed to planetary effects. We thus argue that it arises from the evolution of the stellar CCF profile during the transit. By applying the SpotCCF tool (Di Maio et al. 2023), we could model the deformation of the CCF profile: assuming differential stellar rotation, we found compatibility with a dark spot

signature, only in the hypothesis that the stellar rotation axis is inclined about 44 degrees from the line of sight. Another possible explanation could be the presence of non-radial stellar pulsations (e.g., Rieutord et al. 2023), despite the star having a relatively low temperature ( $T_{\text{eff}} \sim 6406$  K). Unfortunately, the time series we have available does not allow us to investigate this further.

We searched for evidence of stellar activity in the TESS LCs. To analyse the photometric variability, we clipped out the in-transit photometry and computed the generalized Lomb-Scargle periodogram (Zechmeister & Kürster 2009; Ferraz-Mello 1981) to detect any periodic signal. We found a clear periodicity at  $\sim 5.4$  days in S24 and S26 (year 2020) with an amplitude of the order of 1 mmag. In S51, S52 and S53 (year 2022) we did not find any clear indication of periodic signals (Fig. 5). As a sanity check, we performed the same analysis using the TESS Simple Aperture Photometry (SAP) and obtained the same results.

Using  $R_*$  indicated by Gully-Santiago et al. (2023) ( $2.65 \pm 0.12 R_{\odot}$ ), and in the scenario of an equator-on star, our estimate of the stellar rotation period leads to an equatorial rotation velocity of  $25 \pm 7 \text{ km s}^{-1}$ . Due to its large uncertainty, this value is consistent inside  $1\sigma$  with the  $v \sin i$  reported by Zhou et al. (2017) ( $30.9 \pm 2 \text{ km s}^{-1}$ ) and within  $2\sigma$  from our derived  $v \sin i$ . This supports the hypothesis that the periodicity of  $\sim 5.4$  d found in the periodogram (Fig. 5) is close to the real stellar rotation period. If, conversely, we assume an inclination of  $\sim 44$  degrees for the stellar rotation axis, then we derive a rotation period of  $\sim 3.7$  d that does not correspond to any clear peak in the periodogram of the TESS photometry. We thus postulate that the star is most likely seen in an equator-on configuration.

## 5. Atmospheric characterization

### 5.1. Extraction of the transmission spectra in the VIS

The standard data reduction in the VIS range is performed using the HARPS-North dedicated DRS, which produces both 2D and 1D spectra. For each night of observation, we analysed the 2D spectra using the SLOppy (Spectral Lines Of Planets with python) pipeline (Sicilia et al. 2022). SLOppy<sup>3</sup> is a user-friendly, standard, and reliable tool that is optimized for spectral reduction and the extraction of planetary transmission spectra in the VIS obtained from high-resolution observations. For this purpose, SLOppy first applies several data reduction steps that are required to correct the input spectra for: *a*) sky emission: the pipeline subtracts the sky spectrum, which is simultaneously retrieved with

<sup>3</sup> <https://github.com/LucaMalavolta/SLOppy>



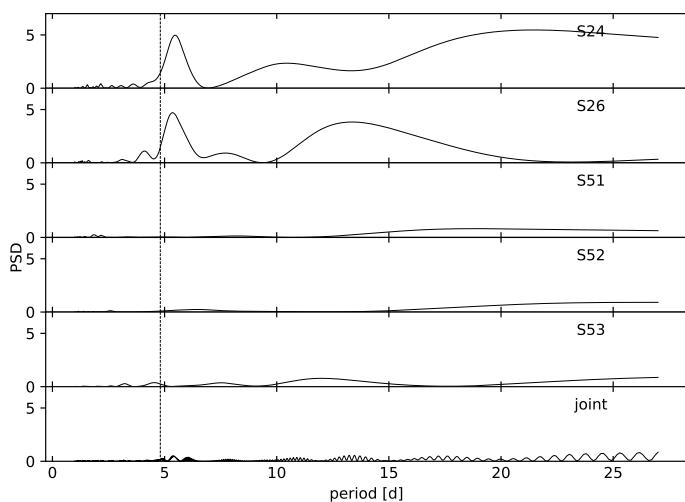


Fig. 5: Generalized Lomb-Scargle periodogram of the five TESS sectors and the joint LC (*bottom box*). The vertical dashed line marks the orbital period of HAT-P-67 b reported in Table 3.

the science observations, from the stellar spectrum (see subSect. 2.1); *b*) atmospheric dispersion: after dividing each observation with a reference spectrum, the pipeline models this ratio with either a low-order polynomial or a spline and finally divides each observation by this model; *c*) the presence of telluric features: among the different approaches implemented in the pipeline, we decided to apply the one that uses the atmospheric transmission code *Molecfit* (Smette et al. 2015; Kausch et al. 2015).

After applying the aforementioned data reduction steps, each in-transit observation is divided by a master-out spectrum ( $M_{\text{out}}$ , i.e., the integration of the exposures out-of-transit acquired before the ingress and after the planet’s egress). In this way, the pipeline removes the stellar contribution and, in principle, the residuals should contain the exoplanet atmospheric signal. The  $M_{\text{out}}$  is built by moving and combining all the out-of-transit spectra to the stellar rest frame. The wavelength shift depends on the barycentric Earth RV (BERV) and the  $v_{\text{sys}}$  of the star. While the BERV values are provided by the DRS in the header of the FITS files, we derived  $v_{\text{sys}}$  ( $-2.234 \pm 0.027 \text{ km s}^{-1}$ ) by taking the weighted average of the two values found from the fit of the RVs of N3 and N4 (we excluded the value found for N1, as it is likely to be contaminated by higher stellar variability, see. Sect. 4).

We did not consider the reflex motion of the star since, being a fast rotator, even a wavelength shift of the order of one pixel (corresponding to an RV shift of  $\sim 0.8 \text{ km s}^{-1}$  in the case of HARPS-N, i.e. the RV variation due to a planet of  $\sim 8 M_J$ ) does not change the shape of the spectrum noticeably due to the large broadening of the spectral lines. Even assuming the planet mass upper limit ( $M_p = 0.59 M_J$ , Zhou et al. 2017), the maximum stellar RV change is  $\sim \pm 0.05 \text{ km s}^{-1}$ ; thus, the out-of-transit spectra can be co-added without taking into account the stellar reflex motion due to the planet ( $K_\star = 0 \text{ km s}^{-1}$ ).

Figure 6 shows  $M_{\text{out}}$  in the region of the sodium doublet, obtained by combining all four nights. The presence of interstellar lines is evident, as expected given its large distance from Earth ( $\sim 320 \text{ pc}$ ). Any small variation of these lines can mimic a false signature; however, not correcting by the stellar reflex motion, and assuming that interstellar lines remain at the same spectral position and totally stable during the night, they would be automatically removed when dividing each spectrum by  $M_{\text{out}}$  in the stellar rest frame (e.g., Casasayas-Barris et al. 2018).

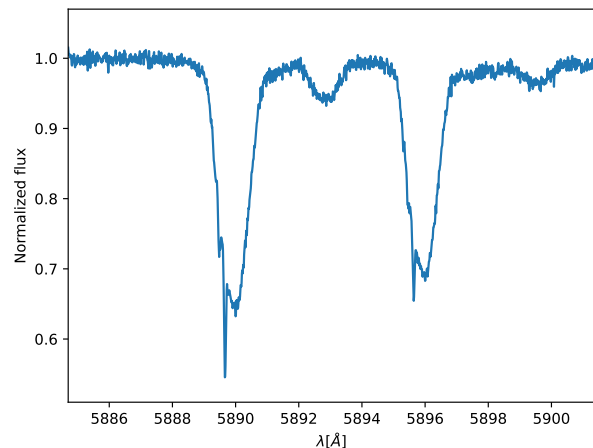


Fig. 6: Composite master-out spectrum normalised to unity around the Na I doublet lines. Deep and narrow interstellar features peak out from the wider stellar lines.

The two main effects altering the transmission spectra, that are the center-to-limb variation (CLV) and the RML effect, are also taken into account (simultaneously). From Spectroscopy Made Easy (SME, Piskunov & Valenti 2017), using a line list from the VALD database (Ryabchikova et al. 2015) and Kurucz ATLAS9 (Kurucz 2005) models, we obtained synthetic stellar spectra at different limb angles (ranging from 0 to 1). SLOppy divides the observed transmission spectrum by a synthetic transmission spectrum computed including the RML and CLV effects in the stellar models, but without the planetary absorption. This step requires the knowledge of some parameters such as the projected spin-orbit angle ( $\lambda$ ), the differential rotation rate ( $\alpha$ ), and the stellar inclination ( $i_\star$ ). As for the first one, for which Zhou et al. (2017) measured an upper limit of  $12^\circ$ , we considered the value found through the tomography method ( $2.2 \pm 0.4^\circ$ ). For most of the stars,  $\alpha$  has not been measured reliably; in this case, the default choice is to exclude the differential rotation in the model and to assume a rigid-body rotation of the star ( $\alpha = 0$ ). Regarding  $i_\star$ , on the other hand, considering what stated in Sect. 4, we expect the star to be close to equator-on ( $i_\star \simeq 90^\circ$ ). Anyway, when rigid-body rotation is assumed, the  $i_\star$  value is not relevant when modelling the CLV and RML effects simultaneously.

## 5.2. Cross-correlation analysis

We investigated the atmospheric composition of HAT-P-67 b using the cross-correlation technique. We used high-resolution model templates at the temperature of 1903 K (Zhou et al. 2017) for the following atoms and molecules: Ca I, Cr I, Fe I, Fe II, H<sub>2</sub>O, K I, Mg I, Na I, Ti I, TiO (using line lists from Exomol and Plez), V I, VO, Y I. The synthetic models of studied species were generated using *petitRADTRANS* (Mollière et al. 2019) assuming equilibrium chemistry, solar abundance from Asplund et al. (2009), and stellar and planetary parameters from Tables 2 and 3. Additionally, in order to simulate the continuum opacity produced by H<sup>-</sup>, we added a cloud layer at  $P_0 = 1 \text{ mbar}$ . In the final step, the high-resolution synthetic spectra were convolved to the HARPS-N resolution using instrumental (Gaussian ker-

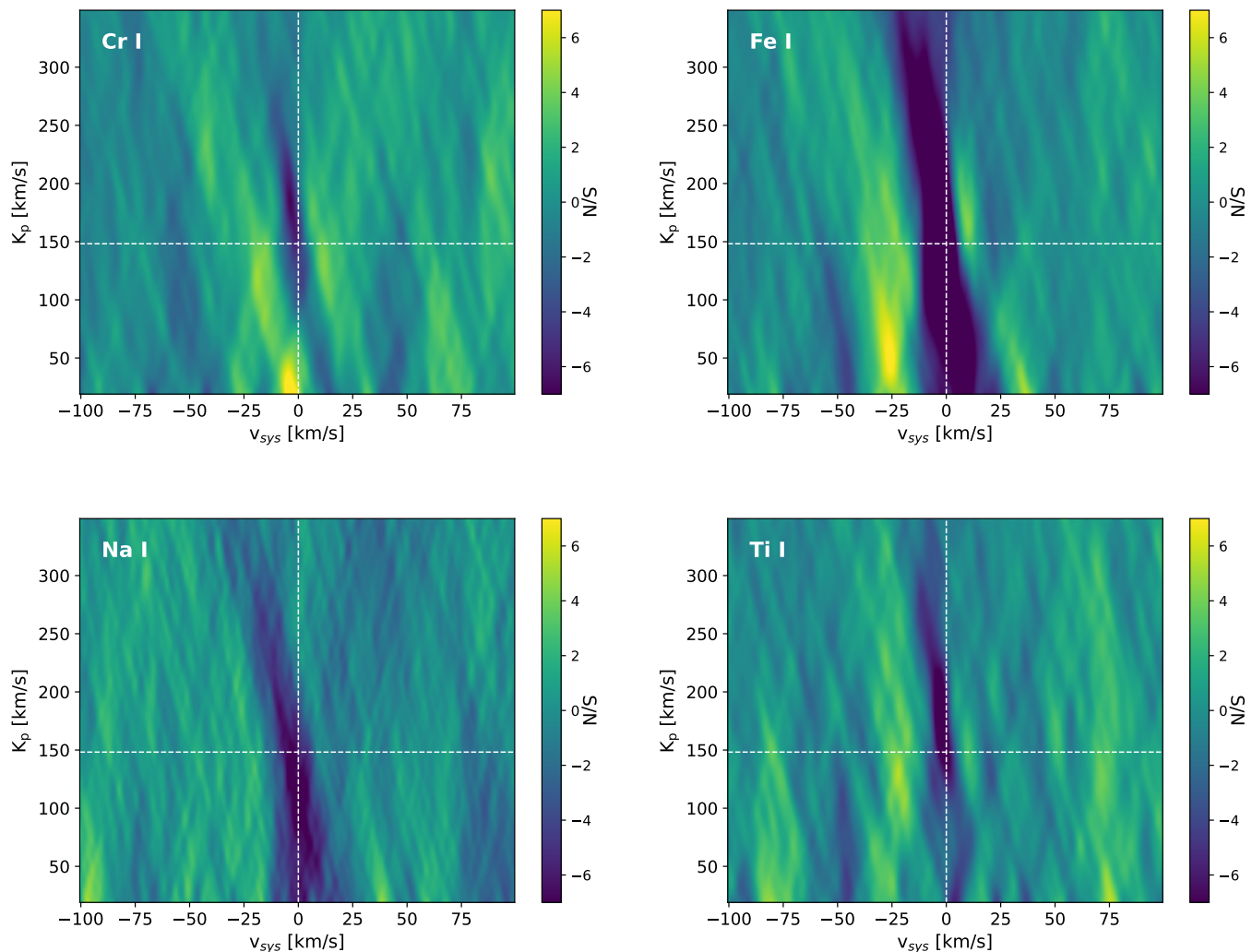


Fig. 7:  $K_p$ - $v_{\text{sys}}$  planes obtained combining all nights for the Cr I (top left), Fe I (top right), Na I (bottom left), and Ti I (bottom right) templates. In each plot, the dashed cross marks the expected  $K_p$  and  $v_{\text{sys}}$  of the system.

nel) broadening `instrBroadGaussFast` from `PyAstronomy`<sup>4</sup> (Czesla et al. 2019).

We cross-correlated the planetary transmission spectra extracted in the VIS range with all the templates listed above, and then combined the CCFs to obtain the  $K_p$ - $v_{\text{sys}}$  maps. We did not detect any robust signal, except for Cr I, Na I, Fe I and Ti I. We remark that these species are commonly found in the transmission spectra of Hot Jupiters (HJs) (see e.g. Hoeijmakers et al. 2018; Ishizuka et al. 2021; Scandariato et al. 2023). The stacked CCFs show, night by night, an absorption feature stretching between the first and fourth contacts ( $t_1$  and  $t_4$ ) and shifting in the velocity space according to the expected planetary keplerian motion (Figs. A.2-A.5). The corresponding  $K_p$ - $v_{\text{sys}}$  maps confirm this evidence by showing a clear absorption feature near the expected  $K_p$  and  $v_{\text{sys}}$  of the system (Fig. 7). Assuming that the median absolute deviation of the  $K_p$ - $v_{\text{sys}}$  maps is a good estimate of the noise, then, the S/N of the absorption features is above 6, 21, 9 and 11 for Cr I, Fe I, Na I and Ti I respectively, when combining all nights.

<sup>4</sup> <https://github.com/sczesla/PyAstronomy>

Since the spectral lines of these atomic species are also present in the stellar spectrum, it is unclear whether these detections are due to either stellar residuals in the transmission spectra or planetary absorption lines. To test the origin of the aforementioned detection we checked whether the stellar spectrum has been effectively removed by the reduction pipeline. To do this, we computed a cross-correlation mask for HAT-P-67 using  $T_{\text{eff}} = 6500$  K,  $\log g = 4.0$ ,  $[\text{Fe}/\text{H}] = 0$  and the theoretical line list provided by the VALD database. Then, we removed all the Cr I, Fe I, Na I and Ti I spectral lines from the mask, in order to leave only the species that do not lead to any detection. Finally, we cross-correlated the transmission spectra, where in the ideal case there should be no signature of the stellar spectrum, with the modified mask. We found that there is a residual trace in the stacked CCFs (Fig. A.6) along the expected position of the planetary absorption which closely follows the stellar Doppler shadow (see Fig. 4). This trace, translated to the  $K_p$ - $v_{\text{sys}}$  plane, generates an absorption feature close to the expected planetary  $K_p$ . The most obvious way to interpret this result is that the stellar spectrum has not been completely removed from the in-transit spectra. To mitigate this problem we tried to re-do the extraction by varying the relevant parameters ( $K_p$ ,  $v \sin i$ ,  $\lambda$ ) within their uncertainties.

Unfortunately, the left-over of the stellar spectrum never faded out.

We thus obtained clear evidence that the removal of the stellar spectrum during the extraction of the transmission spectra is unable to completely remove the stellar signature, casting serious doubts on the reliability of the planetary Cr I, Fe I, Na I and Ti I detections seen in transmission. This does not exclude the fact that a genuine planetary signal exists. Unfortunately, however, the fact that the planetary trace is expected to follow the Doppler shadow complicates the unequivocal attribution of the signal.

### 5.3. Transmission spectroscopy of the H-alpha line with HARPS-N

As already mentioned, recently, the atmosphere of HAT-P-67 b has been explored by Bello-Arufe et al. (2023), through the analysis of one full transit retrieved with CARMENES. In addition to the detection of Na I, which they ascribe to the planetary signal, they also reported a strong absorption near the H-alpha ( $H\alpha$ ), the first spectral line in the Balmer series. We searched for the same signal in our optical transmission spectra ( $\mathfrak{R}$ ) extracted from SLOPPy (see subSect. 5.1), by summing all in-transit observations divided by the  $M_{\text{out}}$  in the planet's reference system. The result for each night is shown in Fig. 8. The analysis reveals the presence of a strong absorption feature in N1, N2, and N3, while a clear emission feature is visible in N4.

For a measure of the absorption signals, we decided to apply an MCMC Gaussian fit in the region of the  $H\alpha$  line. A summary of the best-fit parameters obtained for each night is reported in Table 4. Combining all nights, we found an absorption signal with a contrast ( $c$ ) of  $\sim 2.2\%$  and a full-width half maximum (FWHM) of  $\sim 38 \text{ km s}^{-1}$ . However, the signal was characterized by a very high red shift ( $\sim 23 \text{ km s}^{-1}$ ) with respect to the predicted line position. We point out that we get compatible results even if setting a prior on  $K_p$  next to the expected value.

Doppler shifts as strong as  $\sim 23 \text{ km/s}$  have never been claimed in the literature. Moreover, global circulation models of the atmospheres of HJs predict the presence of zonal winds flowing from the planetary dayside to the nightside (e.g., Komacek & Showman 2016; Parmentier & Crossfield 2018; Roman et al. 2021); this would lead to a blue shifted atmospheric signal, in contrast with our finding. We thus postulate that the planetary origin of the  $H\alpha$  absorption signal is unlikely. Nonetheless, a more thorough investigation, beyond the scope of this paper, is needed to give an appropriate interpretation of the absorption feature seen during the transits.

Regarding N4, as explained in Appendix B, we found that the emission feature originates from around mid-transit and seems to be at rest in the stellar reference system. As shown in Fig. 3, N4 presents higher variability in the chromospheric activity index  $\log R'_{\text{HK}}$  right at the centre of the transit until the end of the observations. This leads us to state that the observed emission signal is probably due to some stellar activity event.

### 5.4. Transmission spectroscopy of the nIR He I triplet with GIANO-B

Similar to the optical analysis, in order to separate the potential planetary He I signal from the stellar contribution, we performed transmission spectroscopy on the GIANO-B spectra using the approach outlined in Guilluy et al. (2023) and Guilluy et al. (2024).

Table 4: Summary of the best-fit parameters and  $1-\sigma$  error bars obtained with the MCMC fitting procedure for the  $H\alpha$  line.

Night	$c$ [%]	FWHM [ $\text{km s}^{-1}$ ]	$v_{\text{wind}}$ [ $\text{km s}^{-1}$ ]
N1	$-2.39^{+0.15}_{-0.15}$	$39.9^{+4.8}_{-4.2}$	$+24.5^{+0.4}_{-0.7}$
N2	$-2.92^{+0.26}_{-0.28}$	$46.0^{+4.7}_{-4.0}$	$+13.1^{+2.1}_{-2.2}$
N3	$-2.29^{+0.22}_{-0.25}$	$42.5^{+6.5}_{-6.2}$	$+20.5^{+2.6}_{-2.6}$
N4	$-1.01^{+0.56}_{-2.23}$	$16.5^{+10.1}_{-15.3}$	$+22.0^{+2.3}_{-9.4}$
Combined	$-2.19^{+0.10}_{-0.10}$	$37.7^{+2.4}_{-2.2}$	$+22.9^{+1.0}_{-1.0}$

We employed the GOFIO pipeline (Rainer et al. 2018) to extract the spectra from the raw GIANO-B images, and a preliminary wavelength calibration using a U-Ne lamp spectrum as a template in the vacuum wavelength frame. We then refined this initial wavelength solution, by employing the same two-steps approach described in our previous works (e.g., Guilluy et al. 2020; Giacobbe et al. 2021), which consists in aligning all the spectra to the Earth's atmospheric rest frame, assuming it as the frame of the observer (disregarding any  $\sim 10 \text{ m s}^{-1}$  differences due to winds). We thus focussed on order #39, which includes the He I triplet.

We employed Molecfit to remove the telluric absorption contamination. Additionally, we masked the emission telluric line at around 1083.43 nm, following the methodology described in Guilluy et al. (2023) and Guilluy et al. (2024).

We moved the telluric-corrected spectra to the stellar rest frame using parameters listed in Tables 3 and 2. We normalised each spectrum to the continuum by median division, neglecting the spectral region near the He I triplet, and excluding spectra with significantly lower signal-to-noise ratios compared to the other exposures. Similar to Gully-Santiago et al. (2023), we then created a master-before, master-in, master-after spectra, by averaging the before- (i.e., with an orbital phase smaller than  $t_1$ ), after- (greater than  $t_4$ ) and in-transit (between  $t_2$  and  $t_3$ ) frames. From the visual comparison of these master spectra, an absorption feature is readily discernible both in the in-transit and before-transit spectra at the position of the He I triplet. This is particularly evident when the nights are considered together (last two panels of Fig. 9). This conspicuous excess absorption ( $\sim 8\%$ ) is visually compatible with what is found in Gully-Santiago et al. (2023) (see their Fig. 8).

Since not all the observed nights provided complete transit coverage, as seen in Fig. A.1, we decided to consider all transits collectively. This is particularly crucial for N1, where the only available comparison stellar spectrum was obtained before the transit. However, considering that Gully-Santiago et al. (2023) identified a helium tail preceding the planet by several hours, we are unable to employ these spectra for comparison due to the potential influence of the planetary tail. In this section, we present the results we obtained by considering only the two nights with the highest S/N, namely N1 and N3. For completeness, the findings obtained for all the investigated nights are illustrated in the Appendix (see Fig. A.7 and Table A.5).

We considered as a comparison spectrum, an average spectrum of all the observations acquired after the transit  $S_{\text{aft}}(\lambda)$ . We thus derived the individual transmission spectra,  $T(\lambda, i)$ , by dividing each spectrum by  $S_{\text{aft}}(\lambda)$ . Finally, we linearly interpolated the transmission spectra in the planet's rest frame. The upper panels of Fig. 10 display the 2D transmission spectroscopy



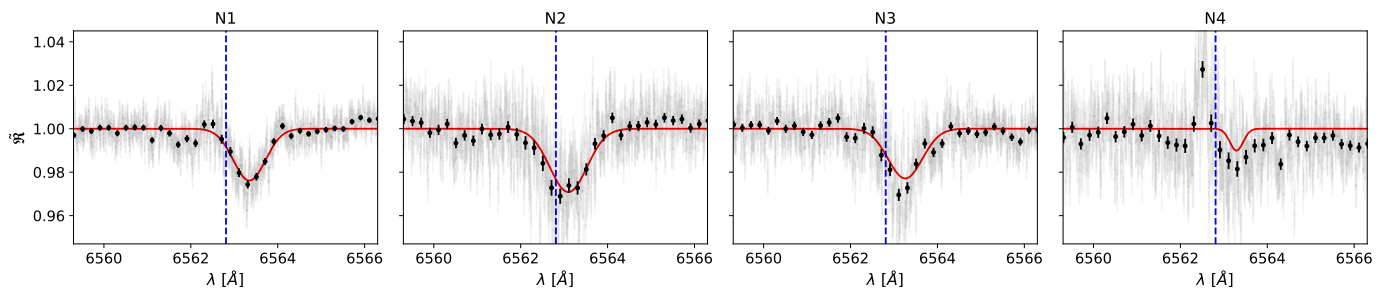


Fig. 8: Transmission spectra of HAT-P-67 b for each night, centered around the H $\alpha$  line in the planetary rest frame (light gray), also binned by 20 $\times$  (in black circles). The red line is the MCMC Gaussian fit performed by SLOppy, while the vertical blue dashed line indicates the rest frame transition wavelength of the H $\alpha$  line.

map in the star (*a* panel) and planet (*b* panel) rest frame, where an absorption signal is visible. With the goal of monitoring the variation of the He I signal during transit, we additionally performed spectrophotometry of the helium triplet within a pass-band of 0.075 nm centered at the peak of excess absorption in the planet rest frame (Allart et al. 2019). The computed transit light curve is presented in the *c*) panel of Fig. 10. We finally obtained the fully in-transit transmission spectrum in the planet’s rest frame  $T_{\text{mean}}(\lambda)$  by averaging the transmission spectra with an orbital phase between  $t_2$  and  $t_3$ .

Following Guilluy et al. (2024), we estimated the contrast  $c$  of the excess absorption at the position of the He I triplet, by fitting a Gaussian profile to  $T_{\text{mean}}(\lambda)$  with the DE-MCMC method varying the peak position, the FWHM, the peak value ( $c$ ), and an offset for the continuum. We also accounted for the presence of correlated noise by using GP regression within the same DE-MCMC tools, using a covariance matrix described by a squared exponential kernel (Bonomo et al. 2023). We finally considered possibly uncorrelated noise by introducing a jitter term  $\sigma_j$ . Panel *d*) of Fig. 10 shows the final  $T_{\text{mean}}$  corrected with the GP model and with overlotted the best-fit Gaussian model. We detected a He I contrast  $c$  of  $5.56^{+0.29}_{-0.30}\%$  at  $19\sigma$ , with a velocity shift of  $v = 10.0^{+1.1}_{-1.2} \text{ km s}^{-1}$ . The best-fit parameters from the DE-MCMC Gaussian analysis are listed in Table 5, while the posterior distribution and the application of the GP model are reported in Appendix in Fig. A.8, and Fig. A.9, respectively.

We then translated  $c$  into an effective planetary radius  $R_{\text{eff}} \sim 3 R_p$  (e.g., Chen et al. 2018), which extension beyond the planet’s Roche Lobe radius ( $2.7 R_p$ , Gully-Santiago et al. 2023) indicates that the planet is evaporating. We found a restricted Jeans escape parameter  $\Lambda \sim 18$  (Fossati et al. 2017). The value obtained supports the presence of an extended atmosphere with significant mass loss, such as one would expect from seeing metastable helium absorption beyond Roche’s lobe. We finally derived the quantity  $\delta_{R_p}/H_{\text{eq}}$  (Nortmann et al. 2018), which represents the number of scale heights probed by the atmosphere in the spectral range under consideration (see Table 5).

We need to be cautious with our He I detection, and emphasize that our measured signal could be contaminated by potential pseudo-signals of stellar activity, caused by the planet’s passage during transit over a non-uniform stellar disk (e.g., Salz et al. 2018; Guilluy et al. 2020, 2024). The variability observed in the H $\alpha$  line (subSect. 5.3), likely attributed to stellar activity, is a warning signal. However, in the He I analysis, we considered all the nights together, primarily due to the absence of post-transit observations in both N1 and N4, which are crucial if a pre-transit tail exists. For this reason, we were unable to analyse possible He I night-to-night variability due to stellar activity.

## 6. Summary and conclusions

HAT-P-67 b is one of the lowest-density exoplanets known to date ( $\rho \sim 0.05 \text{ g cm}^{-3}$ ), making it a prime target for transmission spectroscopy. In the framework of the GAPS programme, we observed four transits of HAT-P-67 b using the GIARPS mode of the TNG, thus aiming at the simultaneous VIS and nIR study of the exoplanet atmosphere.

Firstly, we derived a new orbital solution for the HAT-P-67 system using archival TESS photometry and found it to be compatible within  $2\sigma$  with Gully-Santiago et al. (2023), who analysed the same TESS sectors. We combined our orbital solution with the RV times series to analyse the RML effect (Rossiter 1924; McLaughlin 1924). From the fit, we estimated the systemic velocity of the system and the projected spin-orbit angle. In order to improve the precision on  $\lambda$ , we applied the Doppler tomographic analysis, finding a value of  $2.2 \pm 0.4^\circ$  when combining all the four transits. Our result is compatible with Zhou et al. (2017), who measured an upper limit of  $12^\circ$  through the same technique. The derived value indicates an aligned planetary orbit and suggests that the planet has likely migrated to its current orbit via tidal interactions with a protoplanetary gas disc (Lin et al. 1996; Ward 1997). It is unlikely that the outer stellar companion is directly involved in the migration of the planet through e.g. Kozai mechanism, because of its very large separation (3400 au); nevertheless, some combinations of the original planetary orbit (e.g.,  $\geq 1 \text{ au}$ ) and binary orbit may allow a phase of high eccentricity and very close periastron followed by tidal circularization on the current orbit within the age of the system. The tidal timescale for the damping of the obliquity, computed for a planetary mass of  $0.32 M_J$  (Gully-Santiago et al. 2023), is of about 0.6 Gyr, while for the mass upper limit of  $0.59 M_J$ , it is of 0.3 Gyr. We have adopted a strong tidal interaction assuming a modified tidal quality factor of the star ( $Q'_*$ ) of  $2.5 \times 10^4$  as in the case of Kepler-1658, another system with a similar subgiant star (Vissapragada et al. 2022). Therefore, an alternative interpretation could be that the planet mass is close to  $0.59 M_J$ , and the low obliquity has been reached only relatively recently, when the star was in the final phase of its main-sequence evolution, and experienced a strong tidal interaction with HAT-P-67 b. This is in agreement also with a stellar rotation period close to the orbital period because tides would act both to damp the obliquity and to synchronize the rotation of the star.

Our first night of observation shows signatures of higher stellar variability than on the other nights analysed. As a matter of fact, compared with the remaining part of our survey, we found an RV offset of  $\sim 200 \text{ m s}^{-1}$ , a higher  $\log R'_{\text{HK}}$  activity index and a distorted CCF profile. Furthermore, although the TESS pho-



Table 5: Best fit parameters from the DE-MCMC Gaussian analysis.

Peak position (nm)	$c$ (%)	$R_{\text{eff}}$ ( $R_p$ )	FWHM (nm)	Significance ( $\sigma$ )	$\delta_{R_p}/H_{\text{eq}}$
$1083.3624^{+0.0041}_{-0.0043}$	$5.56^{+0.29}_{-0.30}$	$3.04 \pm 0.07$	$0.1701^{+0.011}_{-0.009}$	19.0	$48.5 \pm 35.8$

**Notes.** From left to right: the peak position of the He I, the absorption (expressed both as contrast  $c$  and  $R_{\text{eff}}$ ), and FWHM obtained from the DE-MCMC analysis, the significance of the detection, and the ratio between the equivalent height of the He I atmosphere and the atmospheric scale height. We determined the values and the  $1\sigma$  uncertainties of the derived parameters from the medians and the 16%-84% quantiles of their posterior distributions.

tometry does not cover our first night of observation, we nevertheless extracted a clear periodicity consistent with stellar rotation from the available TESS LCs, spanning a period fairly close to that observed. By modelling the CCF profiles, we found that the stellar variability observed does not appear to be due to stellar spots, which would have generated a different periodicity than what was instead extracted from TESS photometry. It is more likely that the source of this variability is related to the presence of non-radial pulsations on the stellar surface.

Using the cross-correlation technique, we searched for the presence of atomic or molecular species in the optical transmission spectrum of HAT-P-67 b. Despite the expected high absorption signal, we did not get any robust detection, with the exception of the Cr I, Fe I, Na I and Ti I, finding a formal statistical significance of  $\sim 6\sigma$ ,  $21\sigma$ ,  $9\sigma$  and  $11\sigma$  respectively in the combined signals. However, when we tested the robustness of the detections (with that of sodium compatible with what is reported by Bello-Arufe et al. 2023), we could not confirm their planetary origin. By carrying out a series of tests, we realised that we were not able to completely remove the stellar contribution from the in-transit spectra, leading to an unreliable transmission signal. After checking that the same analysis technique works well on other targets with clear detections (e.g. KELT-20 b), our assumption is that the models used for the data reduction, especially the removal of the contribution of the RML and CLV effects, poorly match the real spectrum of HAT-P-67. The use of 3D models could improve the characterization of the exoplanetary atmosphere. Evidence for this was recently reported by Canocchi et al. (2023), who applied 3D non-LTE synthetic spectra to estimate the stellar RM+CLV effects in transmission spectra of solar-like planet hosts, showing that 1D models seem to overestimate the CLV signature. Even earlier, Chiavassa & Brogi (2019) showed that removing the stellar spectrum using 3D radiative hydrodynamical simulations leads to a significant improvement in planet detectability, both in solar-type and K-dwarf stars.

Due to the strong irradiation from the host star combined with internal heating within the planet, and its very low escape velocity ( $v_{\text{esc}} \sim 25 \text{ km s}^{-1}$ , Zhou et al. 2017), HAT-P-67 b's atmosphere has been undergoing an intense radius inflation; this should have led to the formation of an extended hydrogen atmosphere. Gas giants with masses below Jupiter, and temperatures above 1800 K, like HAT-P-67 b ( $T_{\text{eq}} \sim 1900 \text{ K}$ ), are so inflated and puffed out that they are all on unstable evolutionary paths which eventually lead to Roche-Lobe overflow and the evaporation and loss of the planet's atmosphere (Batygin et al. 2011). In the VIS wavelength range, the H $\alpha$  line is a powerful probe of the escaping atmosphere (Yan & Henning 2018; Borsa et al. 2021a; Czesla et al. 2022). On HAT-P-67 b, our results for the first three nights analysed are compatible with what found by Bello-Arufe et al. (2023), that is a highly red shifted ( $\sim 23 \text{ km/s}$ ) strong absorption signal ( $\sim 2.5\%$ ); however, this finding is un-

pected by the current global circulation models of HJs. We thus argue that such an absorption signal can be hardly ascribed to planetary origin. Only for the last night of observations, we find a clear emission signal in the transmission spectrum; the correlation with the chromospheric index  $\log R'_{\text{HK}}$  leads us to think that the origin of the emission feature is most likely stellar activity.

Gully-Santiago et al. (2023) found no detectable variability in other hydrogen lines, but confirmed the presence of a large and variable He I tail preceding the planet. Thanks to the GIARPS observing mode of the TNG, we were able to extract the transmission spectrum in the region of the nIR He I triplet. Using the average of all the spectra acquired after the transit as the master-out spectrum, we found a clear absorption signal. Applying a Gaussian fit to the full in-transit mean transmission spectrum, we estimated a contrast of the excess absorption of  $5.56^{+0.29}_{-0.30}\%$  ( $19.0\sigma$ ). This value corresponds to an effective planetary radius of  $\sim 3 R_p$  ( $\sim 6 R_J$ ), indicating that the planet's atmosphere is evaporating. Assuming a scale height ( $H$ ) of  $\sim 3500 \text{ km}$ , and considering  $1\sigma$  uncertainties, we found that the He I atmosphere probes a number of scale heights varying between  $\sim 13$  and  $\sim 84 H$ .

In conclusion, despite HAT-P-67 b is one of the most favorable target for transmission spectroscopy studies, there are factors, such as stellar variability and observational constraints (i.e., the long transit duration), that make analysis challenging and, therefore, less accurate. Furthermore, the fact that the orbital trace of the planet is almost identical to that of the Doppler shadow complicates the unequivocal attribution of the signal found to either planet or star.

*Acknowledgements.* The authors acknowledge financial contribution from PRIN INAF 2019 and from the European Union - Next Generation EU RRF M4C2 1.1 PRIN MUR 2022 project 2022CERJ49 (ESPLORA). We thank the anonymous referee for their thoughtful comments which helped to improve the quality of this work. This paper includes data collected by the TESS mission, which are publicly available from the Mikulsky Archive for Space Telescopes (MAST). Funding for the TESS mission is provided by the NASA's Science Mission directorate. D.S. thanks L. Pino for discussions and insights. L. M. acknowledges support from the MIUR-PRIN project No. 2022J4H55R.

## References

- Albrecht, S. H., Dawson, R. I., & Winn, J. N. 2022, *PASP*, 134, 082001  
Allart, R., Bourrier, V., Lovis, C., et al. 2019, *A&A*, 623, A58  
Allart, R., Pino, L., Lovis, C., et al. 2020, arXiv e-prints, arXiv:2010.15143  
Anderson, D. R., Hellier, C., Gillon, M., et al. 2010, *ApJ*, 709, 159  
Apai, D., Rackham, B. V., Giampapa, M. S., et al. 2018, arXiv e-prints, arXiv:1803.08708  
Asplund, M., Grevesse, N., Sauval, A. J., & Scott, P. 2009, *ARA&A*, 47, 481  
Batygin, K., Stevenson, D. J., & Bodenheimer, P. H. 2011, *ApJ*, 738, 1  
Bello-Arufe, A., Knutson, H. A., Mendonça, J. M., et al. 2023, arXiv e-prints, arXiv:2307.06356  
Bertocco, S., Goz, D., Tornatore, L., et al. 2020, in *Astronomical Society of the Pacific Conference Series*, Vol. 527, *Astronomical Data Analysis Software and Systems XXIX*, ed. R. Pizzo, E. R. Deul, J. D. Mol, J. de Plaa, & H. Verkouter, 303

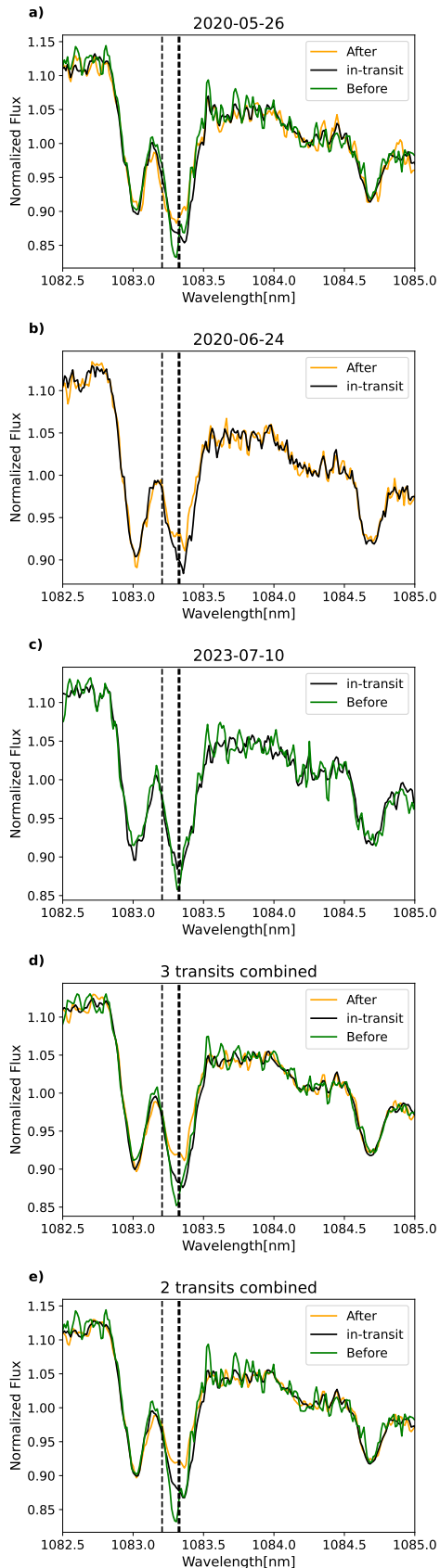


Fig. 9: Master-after, master-before, and master-in spectra in the star frame. a), b), and c) panels represent the GIANO-B nights considered individually. Panel d) shows all three transits together, while in panel e) only the two observations with the highest S/N are considered. Vertical lines indicate the position of the He I. In- and before-transit absorption is visible by eye.

- Bonomo, A. S., Dumusque, X., Massa, A., et al. 2023, *A&A*, 677, A33
- Borsa, F., Allart, R., Casasayas-Barris, N., et al. 2021a, *A&A*, 645, A24
- Borsa, F., Lanza, A. F., Raspantini, I., et al. 2021b, *A&A*, 653, A104
- Brown, T. M. 2001, *ApJ*, 553, 1006
- Canocchi, G., Lind, K., Lagae, C., et al. 2023, arXiv e-prints, arXiv:2312.05078
- Casasayas-Barris, N., Pallé, E., Yan, F., et al. 2018, *A&A*, 616, A151
- Chen, G., Pallé, E., Welbanks, L., et al. 2018, *A&A*, 616, A145
- Chiavassa, A. & Brogi, M. 2019, *A&A*, 631, A100
- Claudi, R., Benatti, S., Carleo, I., et al. 2018, in *Society of Photo-Optical Instrumentation Engineers (SPIE) Conference Series*, Vol. 10702, *Ground-based and Airborne Instrumentation for Astronomy VII*, ed. C. J. Evans, L. Simard, & H. Takami, 107020Z
- Colón, K. D., Kreidberg, L., Welbanks, L., et al. 2020, *AJ*, 160, 280
- Cosentino, R., Lovis, C., Pepe, F., et al. 2012, in *Society of Photo-Optical Instrumentation Engineers (SPIE) Conference Series*, Vol. 8446, *Ground-based and Airborne Instrumentation for Astronomy IV*, ed. I. S. McLean, S. K. Ramsay, & H. Takami, 84461V
- Covino, E., Esposito, M., Barbieri, M., et al. 2013, *A&A*, 554, A28
- Czesla, S., Lampón, M., Sanz-Forcada, J., et al. 2022, *A&A*, 657, A6
- Czesla, S., Schröter, S., Schneider, C. P., et al. 2019, *PyA: Python astronomy-related packages*, *Astrophysics Source Code Library*, record ascl:1906.010
- Di Maio, C., Petralia, A., Micela, G., et al. 2023, arXiv e-prints, arXiv:2312.14269
- Dumusque, X., Lovis, C., Udry, S., & Santos, N. C. 2011, in *The Astrophysics of Planetary Systems: Formation, Structure, and Dynamical Evolution*, ed. A. Sozzetti, M. G. Lattanzi, & A. P. Boss, Vol. 276, 530–532
- Eastman, J. 2017, *EXOFASTv2: Generalized publication-quality exoplanet modeling code*, *Astrophysics Source Code Library*, record ascl:1710.003
- Eastman, J., Gaudi, B. S., & Agol, E. 2013, *PASP*, 125, 83
- Egeland, R., Soon, W., Baliunas, S., et al. 2017, *The Astrophysical Journal*, 835, 25
- Esposito, M., Covino, E., Desidera, S., et al. 2017, *A&A*, 601, A53
- Ferraz-Mello, S. 1981, *AJ*, 86, 619
- Foreman-Mackey, D., Hogg, D. W., Lang, D., & Goodman, J. 2013, *PASP*, 125, 306
- Fossati, L., Ingrassia, S., & Lanza, A. F. 2015, *The Astrophysical Journal Letters*, 812, L35
- Fossati, L., Marcelja, S. E., Staab, D., et al. 2017, *A&A*, 601, A104
- Giacobbe, P., Brogi, M., Gandhi, S., et al. 2021, *Nature*, 592, 205
- Goodman, J. & Weare, J. 2010, *Communications in Applied Mathematics and Computational Science*, 5, 65
- Guilluy, G., Andretta, V., Borsa, F., et al. 2020, *A&A*, 639, A49
- Guilluy, G., Bourrier, V., Jaziri, Y., et al. 2023, *A&A*, 676, A130
- Guilluy, G., D’Arpa, M. C., Bonomo, A. S., et al. 2024, arXiv e-prints, arXiv:2403.00608
- Guilluy, G., Giacobbe, P., Carleo, I., et al. 2022, *A&A*, 665, A104
- Gully-Santiago, M., Morley, C. V., Luna, J., et al. 2023, arXiv e-prints, arXiv:2307.08959
- Hoeijmakers, H. J., Ehrenreich, D., Heng, K., et al. 2018, *Nature*, 560, 453
- Hunter, A. A., Macgregor, A. B., Szabo, T. O., & et al. 2012, *SourceCodeBioMed*, 7, 1
- Ishizuka, M., Kawahara, H., Nugroho, S. K., et al. 2021, *AJ*, 161, 153
- Kausch, W., Noll, S., Smette, A., et al. 2015, *A&A*, 576, A78
- Kipping, D. M. 2013, *MNRAS*, 435, 2152
- Komacek, T. D. & Showman, A. P. 2016, *ApJ*, 821, 16
- Kurucz, R. L. 2005, *Memorie della Societa Astronomica Italiana Supplementi*, 8, 14
- Lam, K. W. F., Faedi, F., Brown, D. J. A., et al. 2017, *A&A*, 599, A3
- Lanza, A. F. 2014, *A&A*, 572, L6
- Lightcurve Collaboration, Cardoso, J. V. d. M., Hedges, C., et al. 2018, *Lightcurve: Kepler and TESS time series analysis in Python*, *Astrophysics Source Code Library*, record ascl:1812.013
- Lin, D. N. C., Bodenheimer, P., & Richardson, D. C. 1996, *Nature*, 380, 606
- Mahadevan, S., Ramsey, L., Bender, C., et al. 2012, in *Society of Photo-Optical Instrumentation Engineers (SPIE) Conference Series*, Vol. 8446, *Ground-based and Airborne Instrumentation for Astronomy IV*, ed. I. S. McLean, S. K. Ramsay, & H. Takami, 84461S
- Mandel, K. & Agol, E. 2002, *ApJ*, 580, L171
- McLaughlin, D. B. 1924, *ApJ*, 60, 22
- Mollière, P., Wardenier, J. P., van Boekel, R., et al. 2019, *A&A*, 627, A67
- Mugrauer, M. 2019, *MNRAS*, 490, 5088
- Nortmann, L., Pallé, E., Salz, M., et al. 2018, *Science*, 362, 1388
- Oshagh, M., Santos, N. C., Ehrenreich, D., et al. 2014, *A&A*, 568, A99
- Parmentier, V. & Crossfield, I. J. M. 2018, in *Handbook of Exoplanets*, ed. H. J. Deeg & J. A. Belmonte, 116
- Pepper, J., Rodriguez, J. E., Collins, K. A., et al. 2017, *The Astronomical Journal*, 153, 215
- Piskunov, N. & Valenti, J. A. 2017, *A&A*, 597, A16

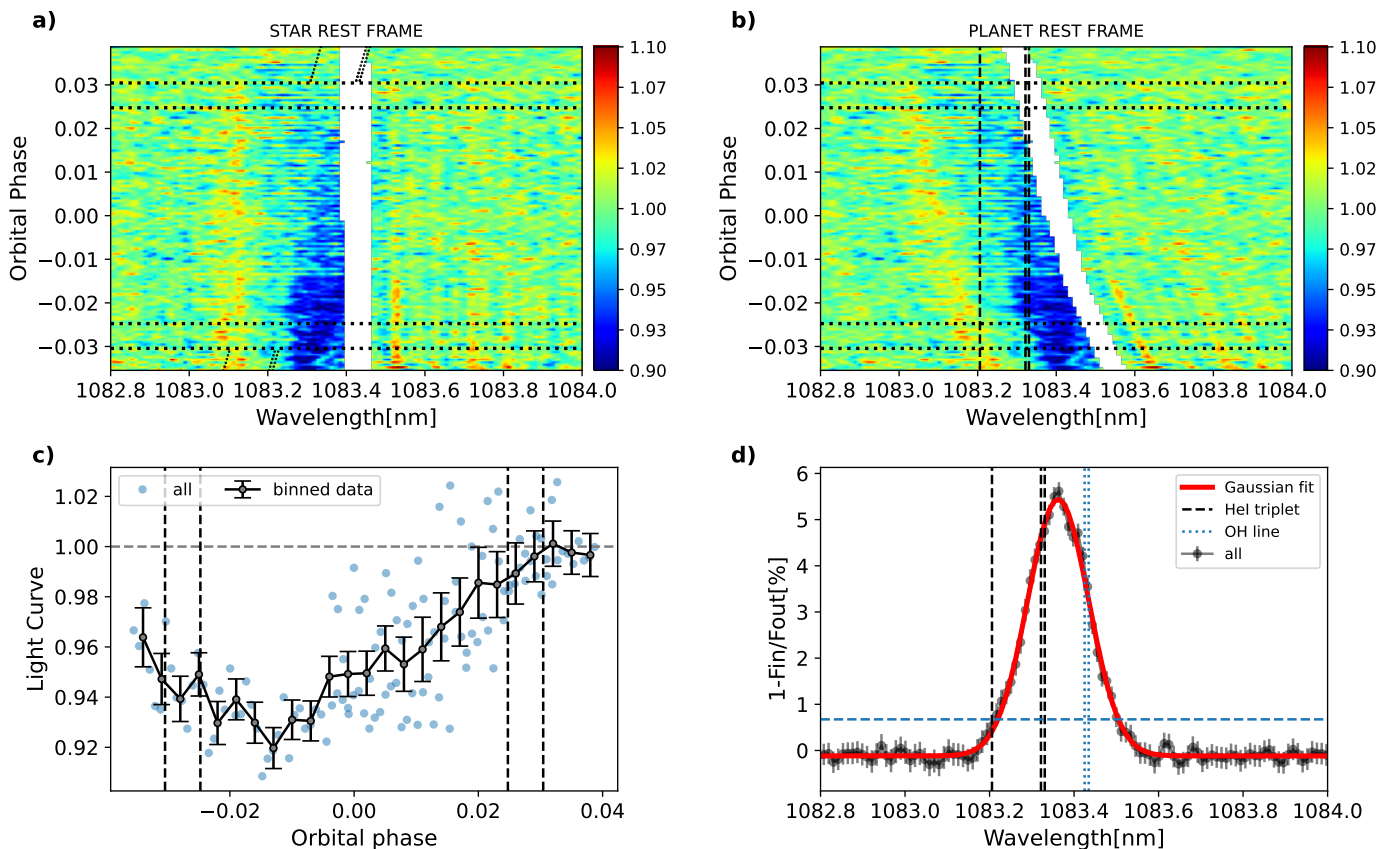


Fig. 10: Transmission spectroscopy near the He I triplet. a) and b) the 2D transmission spectroscopy maps in the stellar and planet rest frames, respectively. Tilted and vertical lines denote the position of the He I triplet, while horizontal dotted lines mark the transit contact points  $t_1$ ,  $t_2$ ,  $t_3$ , and  $t_4$ . c) the spectroscopic light curve computed in a 0.075 nm band centered around the peak of absorption. Vertical dashed lines mark the transit contact points. d) the full in-transit averaged transmission spectrum.

- Quirrenbach, A., Amado, P. J., Caballero, J. A., et al. 2016, Society of Photo-Optical Instrumentation Engineers (SPIE) Conference Series, Vol. 9908, CARMENES: an overview six months after first light, 990812
- Rainer, M., Harutyunyan, A., Carleo, I., et al. 2018, in Society of Photo-Optical Instrumentation Engineers (SPIE) Conference Series, Vol. 10702, Ground-based and Airborne Instrumentation for Astronomy VII, 1070266
- Ricker, G. R., Winn, J. N., Vanderspek, R., et al. 2014, in Society of Photo-Optical Instrumentation Engineers (SPIE) Conference Series, Vol. 9143, Space Telescopes and Instrumentation 2014: Optical, Infrared, and Millimeter Wave, ed. J. Oschmann, Jacobus M., M. Clampin, G. G. Fazio, & H. A. MacEwen, 914320
- Rieutord, M., Petit, P., Reese, D., et al. 2023, A&A, 669, A99
- Roman, M. T., Kempton, E. M. R., Rauscher, E., et al. 2021, ApJ, 908, 101
- Rossiter, R. A. 1924, ApJ, 60, 15
- Ryabchikova, T., Piskunov, N., Kurucz, R. L., et al. 2015, Phys. Scr, 90, 054005
- Salz, M., Czesla, S., Schneider, P. C., et al. 2018, A&A, 620, A97
- Scandariato, G., Borsa, F., Bonomo, A. S., et al. 2023, A&A, 674, A58
- Scandariato, G., Singh, V., Kitzmann, D., et al. 2022, arXiv e-prints, arXiv:2209.05303
- Sedaghati, E., Boffin, H. M. J., Jeřabková, T., et al. 2016, A&A, 596, A47
- Sicilia, D., Malavolta, L., Pino, L., et al. 2022, A&A, 667, A19
- Smette, A., Sana, H., Noll, S., et al. 2015, A&A, 576, A77
- Smith, J. C., Stumpe, M. C., Van Cleve, J., et al. 2012, in American Astronomical Society Meeting Abstracts, Vol. 220, American Astronomical Society Meeting Abstracts #220, 330.03
- Stumpe, M. C., Smith, J. C., Catanzarite, J. H., et al. 2014, PASP, 126, 100
- Stumpe, M. C., Smith, J. C., Van Cleve, J. E., et al. 2012, PASP, 124, 985
- Taffoni, G., Becciani, U., Garilli, B., et al. 2020, in Astronomical Society of the Pacific Conference Series, Vol. 527, Astronomical Data Analysis Software and Systems XXIX, ed. R. Pizzo, E. R. Deul, J. D. Mol, J. de Plaa, & H. Verkouter, 307
- Ter Braak, C. J. F. 2006, Statistics and Computing, 16, 239
- Vissapragada, S., Chontos, A., Greklek-McKeon, M., et al. 2022, The Astrophysical Journal Letters, 941, L31
- Ward, W. R. 1997, Icarus, 126, 261
- Yan, F. & Henning, T. 2018, Nature Astronomy, 2, 714
- Zechmeister, M. & Kürster, M. 2009, A&A, 496, 577
- Zhou, G., Bakos, G. A., Hartman, J. D., et al. 2017, AJ, 153, 211

## Appendix A: Additional Figures and Tables

### Appendix B: Cross-correlation analysis of the H $\alpha$ line

The transmission spectrum of the H $\alpha$  line reveals the presence of a clear emission feature during N4 (see Fig. 8). Trying to understand the origin of this feature, we replicated the same CCF analysis discussed in Sect. 5.2 by creating a binary mask containing only the H $\alpha$  line. The result for each night is shown in Fig. B.1. As expected, the cross-correlation analysis reveals the presence of a strong absorption feature in N1, N2, and N3, well-aligned in the stellar rest frame, with a S/N above 5 in all three nights. Besides, the peaks of these signals are not in correspondence with the expected  $K_p$  of the system. From the cross-correlation analysis of N4, we can see the emission feature starting from around mid-transit. Moreover, even on this night, the signal does not follow the track expected by the planet, but is well aligned in the stellar reference system.



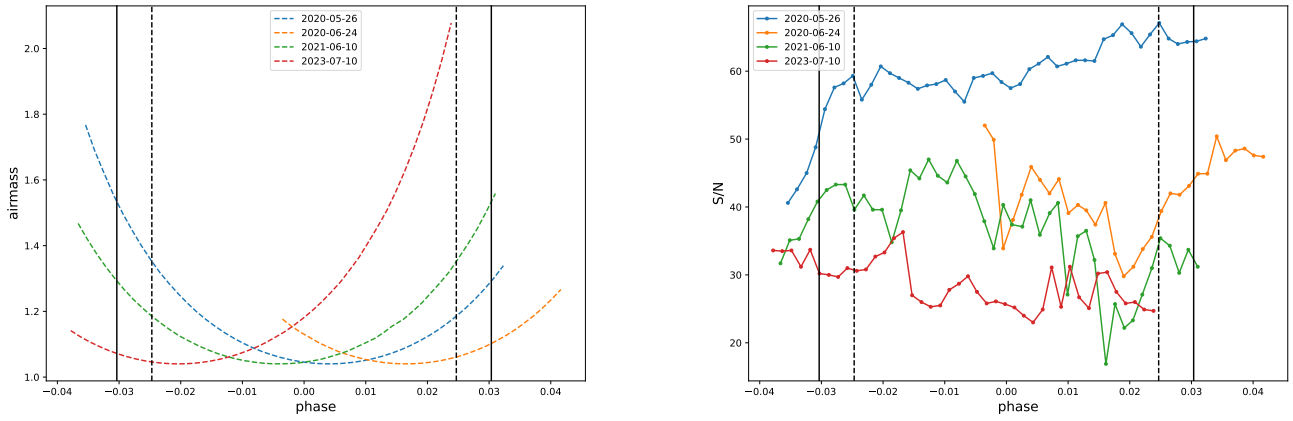


Fig. A.1: Variation of airmass (*left*) and signal-to-noise ratio (S/N) (*right*) for each night of HAT-P-67 b. The S/N is extracted from the FITS header of the HARPS-N spectra on the 53rd order that contains the sodium feature. The continuous and the dashed vertical black lines represent the four points of contact of the transit.

Table A.1: Time series of HAT-P-67 b from HARPS-N data of night 2020-05-26: BJD, RVs, and the  $\log R'_{\text{HK}}$  values with their related uncertainties.

BJD	RV [km s <sup>-1</sup> ]	$\sigma_{\text{RV}}$ [km s <sup>-1</sup> ]	$\log R'_{\text{HK}}$	$\sigma_{\log R'_{\text{HK}}}$
2458996.390744	-2.186	0.025	-4.6316	0.0163
2458996.397862	-2.084	0.025	-4.6250	0.0145
2458996.405362	-2.029	0.024	-4.6335	0.0135
2458996.412387	-2.013	0.023	-4.6287	0.0116
2458996.419644	-2.007	0.022	-4.6314	0.0096
2458996.426994	-2.007	0.022	-4.6295	0.0087
2458996.434193	-1.942	0.021	-4.6316	0.0085
2458996.441369	-1.921	0.022	-4.6435	0.0083
2458996.448417	-1.891	0.022	-4.6426	0.0092
2458996.455802	-1.826	0.021	-4.6328	0.0084
2458996.463186	-1.877	0.021	-4.6411	0.0078
2458996.470350	-1.767	0.021	-4.6535	0.0081
2458996.477480	-1.832	0.021	-4.6520	0.0082
2458996.484806	-1.824	0.021	-4.6533	0.0082
2458996.492086	-1.833	0.021	-4.6442	0.0085
2458996.499309	-1.815	0.022	-4.6626	0.0087
2458996.506531	-1.765	0.021	-4.6540	0.0083
2458996.513823	-1.820	0.021	-4.6493	0.0081
2458996.521149	-1.817	0.021	-4.6398	0.0082
2458996.528348	-1.886	0.021	-4.6638	0.0091
2458996.535721	-1.906	0.020	-4.6635	0.0080
2458996.542908	-1.875	0.021	-4.6613	0.0077
2458996.550211	-1.945	0.020	-4.6642	0.0076
2458996.557329	-1.992	0.021	-4.6528	0.0075
2458996.564471	-1.991	0.021	-4.6622	0.0078
2458996.571878	-2.074	0.020	-4.6629	0.0076
2458996.579100	-2.108	0.020	-4.6555	0.0070
2458996.586334	-2.097	0.019	-4.6500	0.0067
2458996.593522	-2.100	0.020	-4.6579	0.0066
2458996.608047	-2.136	0.020	-4.6531	0.0069
2458996.600767	-2.181	0.019	-4.6597	0.0069
2458996.615258	-2.209	0.019	-4.6546	0.0068
2458996.622549	-2.161	0.020	-4.6763	0.0072
2458996.629853	-2.110	0.020	-4.6540	0.0070
2458996.637063	-2.098	0.019	-4.6596	0.0065
2458996.644309	-2.131	0.020	-4.6583	0.0065
2458996.651461	-2.050	0.019	-4.6569	0.0062
2458996.658799	-2.127	0.020	-4.6521	0.0065
2458996.666079	-2.051	0.020	-4.6468	0.0069
2458996.673186	-2.061	0.020	-4.6665	0.0069
2458996.680397	-1.963	0.019	-4.6463	0.0064
2458996.687700	-2.002	0.020	-4.6380	0.0067
2458996.694899	-1.964	0.020	-4.6517	0.0067
2458996.702179	-1.915	0.020	-4.6405	0.0066
2458996.709447	-1.946	0.020	-4.6377	0.0066
2458996.716647	-1.945	0.020	-4.6367	0.0067

Table A.2: As Table A.1 but for night 2020-06-24.

BJD	RV [km s <sup>-1</sup> ]	$\sigma_{RV}$ [km s <sup>-1</sup> ]	$\log R'_{HK}$	$\sigma_{\log R'_{HK}}$
2459025.404989	-1.841	0.024	-4.6748	0.0104
2459025.411922	-1.870	0.023	-4.6773	0.0113
2459025.419317	-2.016	0.028	-4.6539	0.0218
2459025.426991	-1.984	0.026	-4.6818	0.0186
2459025.433773	-1.912	0.025	-4.7076	0.0165
2459025.441180	-2.022	0.024	-4.6857	0.0132
2459025.448078	-2.024	0.025	-4.6857	0.0144
2459025.455462	-2.111	0.026	-4.6775	0.0155
2459025.462800	-2.164	0.024	-4.6877	0.0143
2459025.470254	-2.147	0.026	-4.7123	0.0183
2459025.477661	-2.151	0.025	-4.7198	0.0175
2459025.484166	-2.096	0.026	-4.6689	0.0162
2459025.491237	-2.076	0.027	-4.6746	0.0181
2459025.499096	-2.108	0.025	-4.6773	0.0154
2459025.506515	-2.124	0.027	-4.6794	0.0225
2459025.513343	-2.113	0.028	-4.6337	0.0248
2459025.520901	-2.000	0.028	-4.6791	0.0254
2459025.528193	-2.051	0.027	-4.6639	0.0224
2459025.535206	-2.098	0.027	-4.6646	0.0205
2459025.542695	-2.082	0.025	-4.6747	0.0171
2459025.549766	-2.040	0.025	-4.6936	0.0160
2459025.556896	-1.976	0.026	-4.6585	0.0148
2459025.564245	-1.907	0.024	-4.6911	0.0150
2459025.571340	-2.028	0.024	-4.6730	0.0134
2459025.578620	-2.009	0.024	-4.6702	0.0133
2459025.585888	-2.013	0.024	-4.6693	0.0114
2459025.593053	-1.941	0.024	-4.6550	0.0128
2459025.600367	-1.938	0.024	-4.6817	0.0129
2459025.607566	-2.089	0.024	-4.6691	0.0124
2459025.614777	-1.980	0.024	-4.6619	0.0128
2459025.622172	-2.006	0.023	-4.6351	0.0122

Table A.3: As Table A.1 but for night 2021-06-10.

BJD	RV [km s <sup>-1</sup> ]	$\sigma_{RV}$ [km s <sup>-1</sup> ]	$\log R'_{HK}$	$\sigma_{\log R'_{HK}}$
2459376.383654	-2.102	0.028	-4.7104	0.0341
2459376.390923	-2.298	0.026	-4.6950	0.0273
2459376.398122	-2.299	0.026	-4.7342	0.0289
2459376.405355	-2.214	0.026	-4.7300	0.0248
2459376.412520	-2.205	0.025	-4.7450	0.0223
2459376.419672	-2.287	0.024	-4.7614	0.0211
2459376.426790	-2.229	0.025	-4.7147	0.0183
2459376.434163	-2.206	0.026	-4.7410	0.0190
2459376.441316	-2.122	0.025	-4.7518	0.0233
2459376.448688	-2.098	0.025	-4.7480	0.0211
2459376.455702	-2.076	0.026	-4.7273	0.0219
2459376.462855	-2.104	0.027	-4.7359	0.0220
2459376.470447	-2.083	0.027	-4.7571	0.0293
2459376.477681	-1.919	0.025	-4.7348	0.0223
2459376.484880	-2.099	0.025	-4.7361	0.0173
2459376.491987	-2.094	0.026	-4.7607	0.0193
2459376.499243	-2.040	0.025	-4.7569	0.0169
2459376.506338	-2.043	0.024	-4.7336	0.0177
2459376.513757	-2.092	0.025	-4.7343	0.0184
2459376.521234	-2.099	0.024	-4.7551	0.0170
2459376.528039	-2.117	0.025	-4.7559	0.0187
2459376.535238	-2.125	0.025	-4.7518	0.0202
2459376.542623	-2.246	0.025	-4.7427	0.0232
2459376.549972	-2.226	0.026	-4.7933	0.0317
2459376.557368	-2.351	0.025	-4.7509	0.0204
2459376.564231	-2.277	0.025	-4.7341	0.0232
2459376.572310	-2.319	0.026	-4.7358	0.0238
2459376.578757	-2.357	0.026	-4.7459	0.0203
2459376.585956	-2.351	0.026	-4.7971	0.0286
2459376.593629	-2.272	0.026	-4.7658	0.0234
2459376.600134	-2.499	0.025	-4.7594	0.0214
2459376.607564	-2.362	0.029	-4.8090	0.0481
2459376.615527	-2.390	0.027	-4.7636	0.0273
2459376.622101	-2.368	0.027	-4.7728	0.0272
2459376.628571	-2.420	0.030	-4.7577	0.0326
2459376.637494	-2.413	0.030	-4.7790	0.0994
2459376.644589	-2.295	0.028	-4.6970	0.0425
2459376.651846	-2.407	0.029	-4.7152	0.0575
2459376.658490	-2.311	0.031	-4.6845	0.0501
2459376.665862	-2.383	0.027	-4.6829	0.0395
2459376.673374	-2.387	0.028	-4.7096	0.0338
2459376.680006	-2.301	0.025	-4.7188	0.0275
2459376.687297	-2.344	0.027	-4.7130	0.0289
2459376.694658	-2.190	0.028	-4.7304	0.0379
2459376.701765	-2.248	0.027	-4.7309	0.0317
2459376.709103	-2.267	0.026	-4.7395	0.0376



Table A.4: As Table A.1 but for night 2023-07-10.

BJD	RV [km s <sup>-1</sup> ]	$\sigma_{RV}$ [km s <sup>-1</sup> ]	$\log R'_{HK}$	$\sigma_{\log R'_{HK}}$
2460136.375287	-2.343	0.027	-4.6775	0.0341
2460136.382428	-2.279	0.028	-4.7147	0.0375
2460136.389615	-2.209	0.027	-4.7254	0.0386
2460136.397011	-2.246	0.027	-4.7191	0.0432
2460136.404233	-2.219	0.027	-4.7187	0.0374
2460136.411455	-2.199	0.027	-4.6715	0.0411
2460136.418769	-2.185	0.029	-4.6722	0.0418
2460136.426026	-2.234	0.027	-4.6940	0.0453
2460136.433213	-2.186	0.027	-4.7258	0.0451
2460136.440540	-2.055	0.028	-4.6986	0.0427
2460136.447715	-2.097	0.028	-4.7120	0.0428
2460136.455042	-2.190	0.027	-4.7177	0.0390
2460136.462148	-2.020	0.028	-4.7273	0.0384
2460136.469567	-2.138	0.026	-4.7484	0.0358
2460136.476592	-2.108	0.025	-4.6923	0.0291
2460136.483687	-2.116	0.028	-4.7060	0.0520
2460136.490990	-1.927	0.029	-4.7164	0.0562
2460136.498177	-2.025	0.030	-4.6803	0.0550
2460136.505642	-1.997	0.027	-4.7121	0.0583
2460136.512725	-2.068	0.027	-4.7339	0.0528
2460136.520260	-2.123	0.028	-4.7696	0.0544
2460136.527297	-2.206	0.029	-4.7307	0.0465
2460136.534299	-2.211	0.028	-4.6749	0.0475
2460136.541868	-2.330	0.030	-4.6974	0.0579
2460136.549044	-2.331	0.029	-4.6806	0.0547
2460136.556196	-2.212	0.028	-4.6933	0.0587
2460136.563511	-2.346	0.029	-4.7877	0.0748
2460136.570814	-2.318	0.029	-4.6262	0.0564
2460136.578059	-2.434	0.030	-4.6700	0.0663
2460136.585571	-2.445	0.029	-4.7495	0.0699
2460136.592561	-2.431	0.027	-4.7155	0.0447
2460136.599934	-2.457	0.029	-4.6655	0.0575
2460136.606751	-2.408	0.028	-4.7594	0.0497
2460136.613996	-2.515	0.030	-4.6555	0.0514
2460136.621611	-2.550	0.029	-4.7017	0.0637
2460136.628706	-2.472	0.027	-4.6684	0.0437
2460136.635824	-2.397	0.029	-4.7512	0.0515
2460136.643023	-2.393	0.029	-4.7921	0.0675
2460136.650291	-2.374	0.029	-4.6927	0.0629
2460136.657467	-2.575	0.028	-4.6626	0.0586
2460136.664735	-2.415	0.029	-4.6351	0.0604
2460136.672027	-2.221	0.029	-4.6254	0.0607

Table A.5: Best fit parameters.

Peak position (nm)	Contrast $c$ (%)	$R_{\text{eff}}$ ( $R_p$ )	FWHM (nm)	Significance ( $\sigma$ )	$\delta_{R_p}/H_{\text{eq}}$
1083.3698 <sup>+0.0045</sup> <sub>-0.0055</sub>	4.56 <sup>+0.32</sup> <sub>-0.31</sub>	2.79 ± 0.08	0.1730 <sup>+0.014</sup> <sub>-0.012</sub>	14.5	42.4 ± 31.3

**Notes.** Same as Table 5, but considering all the available GIANO-B nights. From left to right: the peak position of the He I, the absorption (expressed both as contrast  $c$  and  $R_{\text{eff}}$ ), and FWHM obtained from the DE-MCMC analysis, the significance of the detection, and the ratio between the equivalent height of the He I atmosphere and the atmospheric scale height. We determined the values and the  $1\sigma$  uncertainties of the derived parameters from the medians and the 16%-84% quantiles of their posterior distributions.

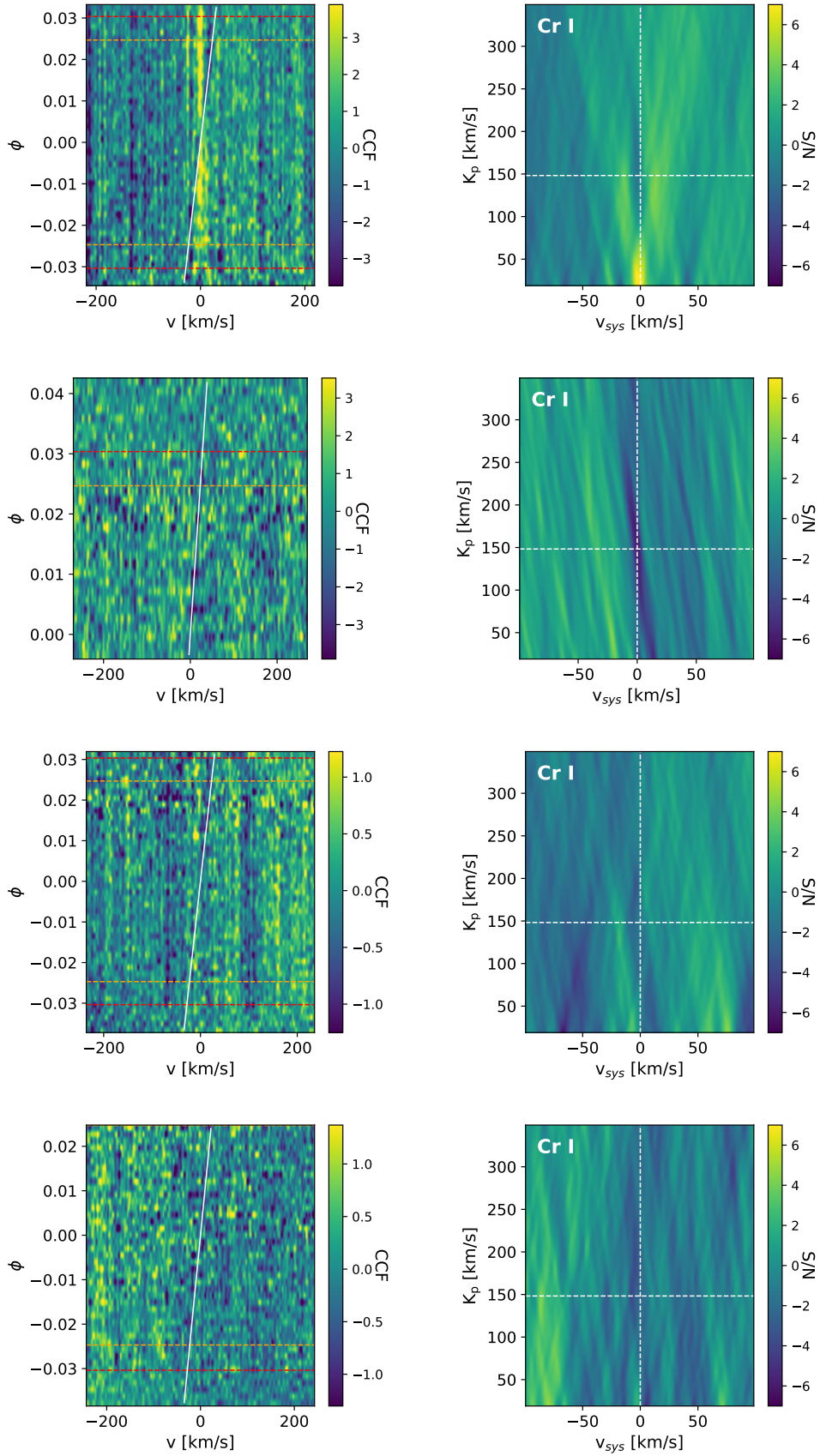


Fig. A.2: *Left column* - Phase-stack of the cross-correlation between the transmission spectra and the Chrome mask. The nights N1, N2, N3 and N4 are shown from top to bottom respectively. In each plot, the orange dashed lines mark the orbital phases corresponding to the second and third contacts. Similarly, the red dashed lines mark the first and fourth contacts. The white solid line traces the expected planetary signal. *Right column* -  $K_p$ - $v_{\text{sys}}$  planes corresponding to the CCFs shown in the left column. In each plot, the dashed cross marks the expected  $K_p$  and  $v_{\text{sys}}$  of the system.

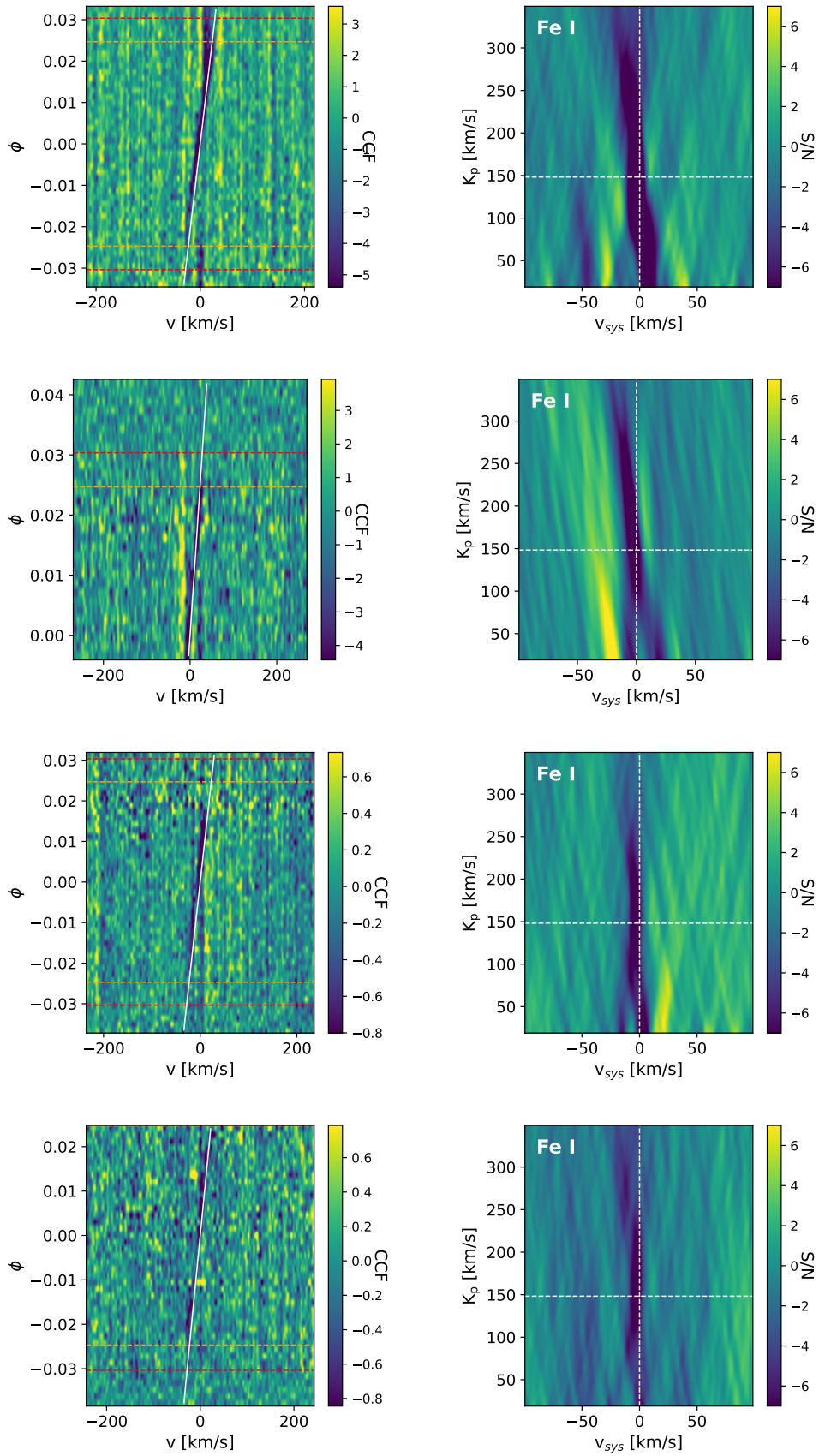


Fig. A.3: As Figure A.2 but for the Fe I mask.

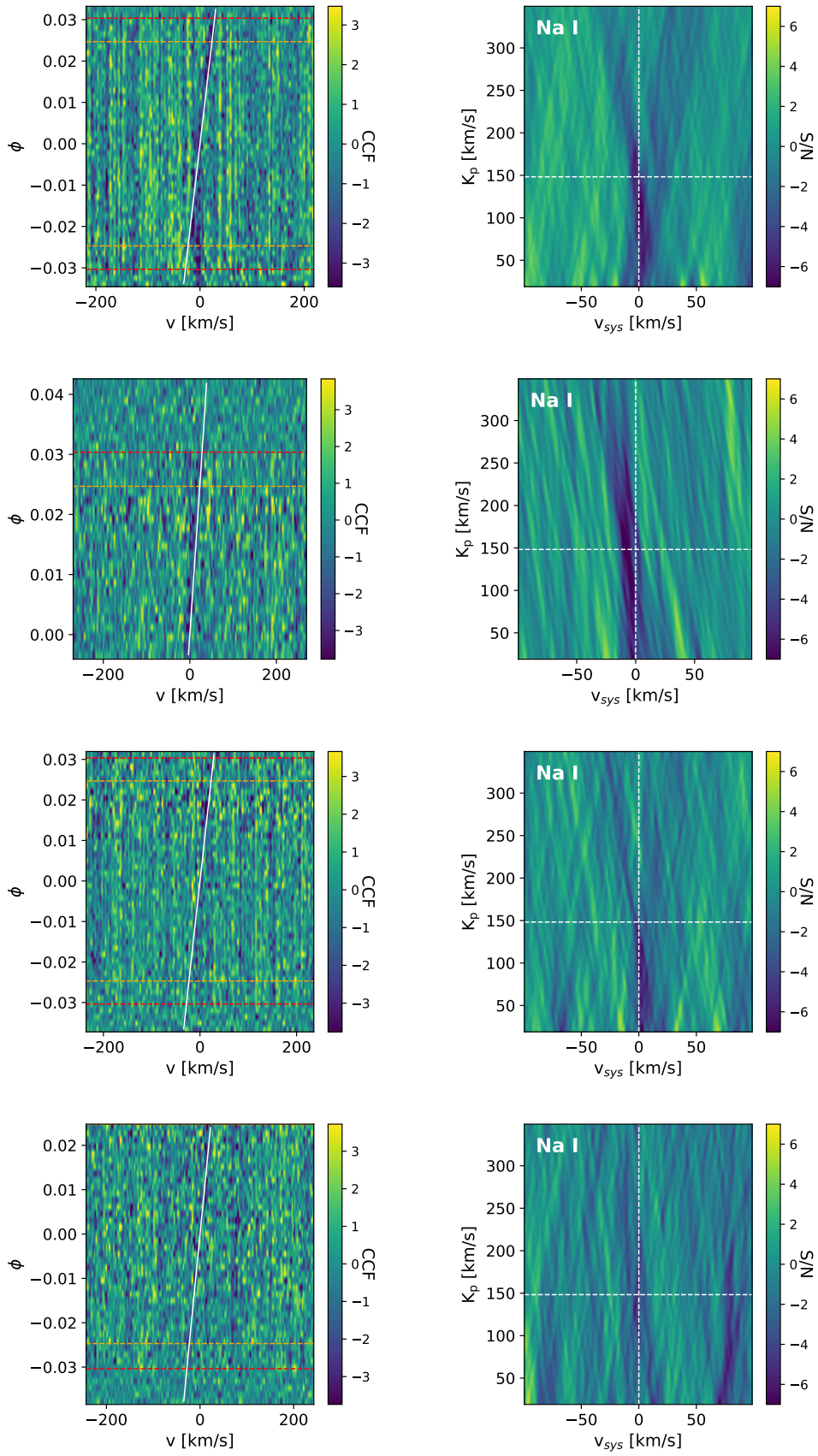


Fig. A.4: As Figure A.2 but for the Na I mask.



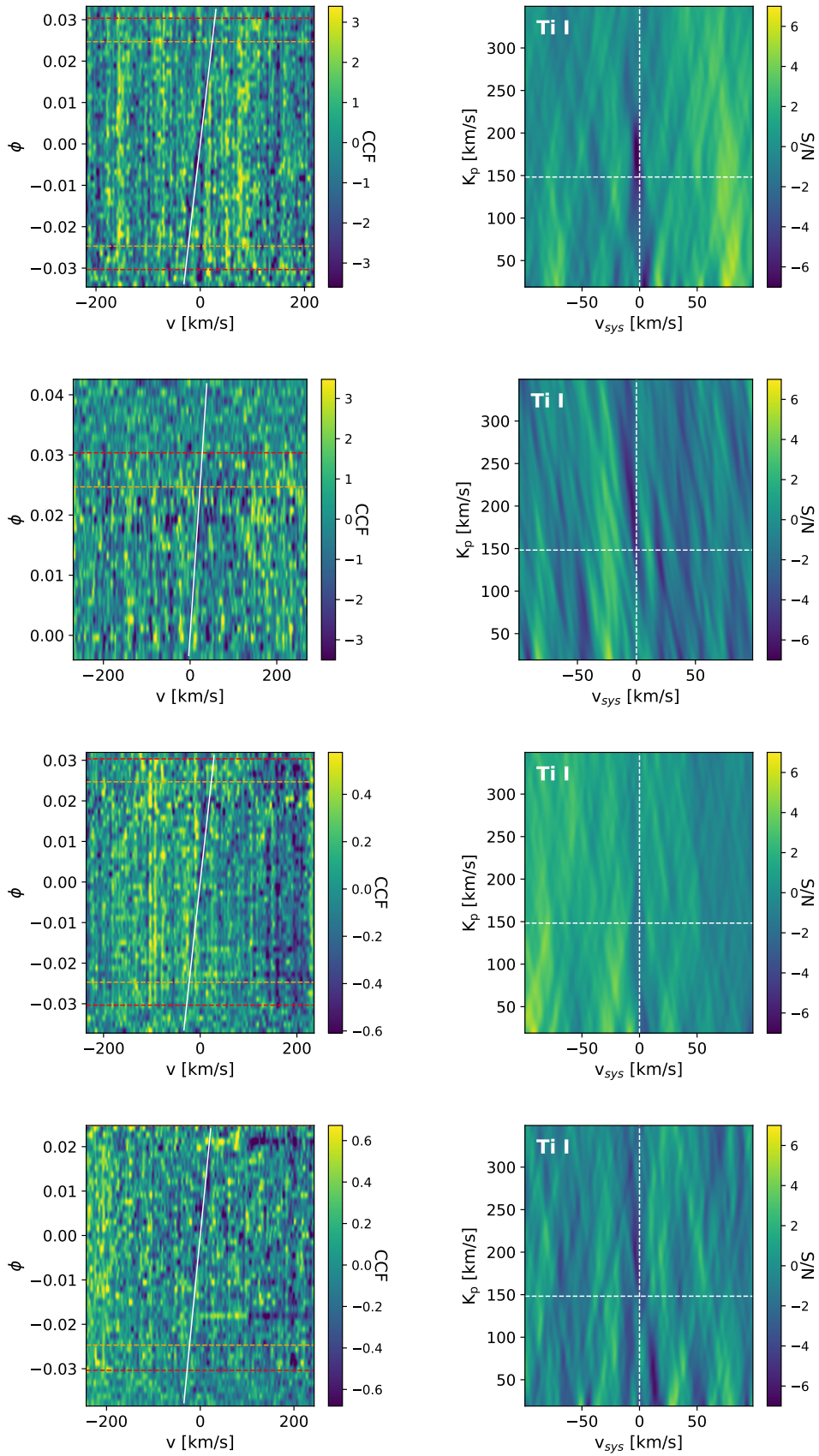


Fig. A.5: As Figure A.2 but for the Ti I mask.

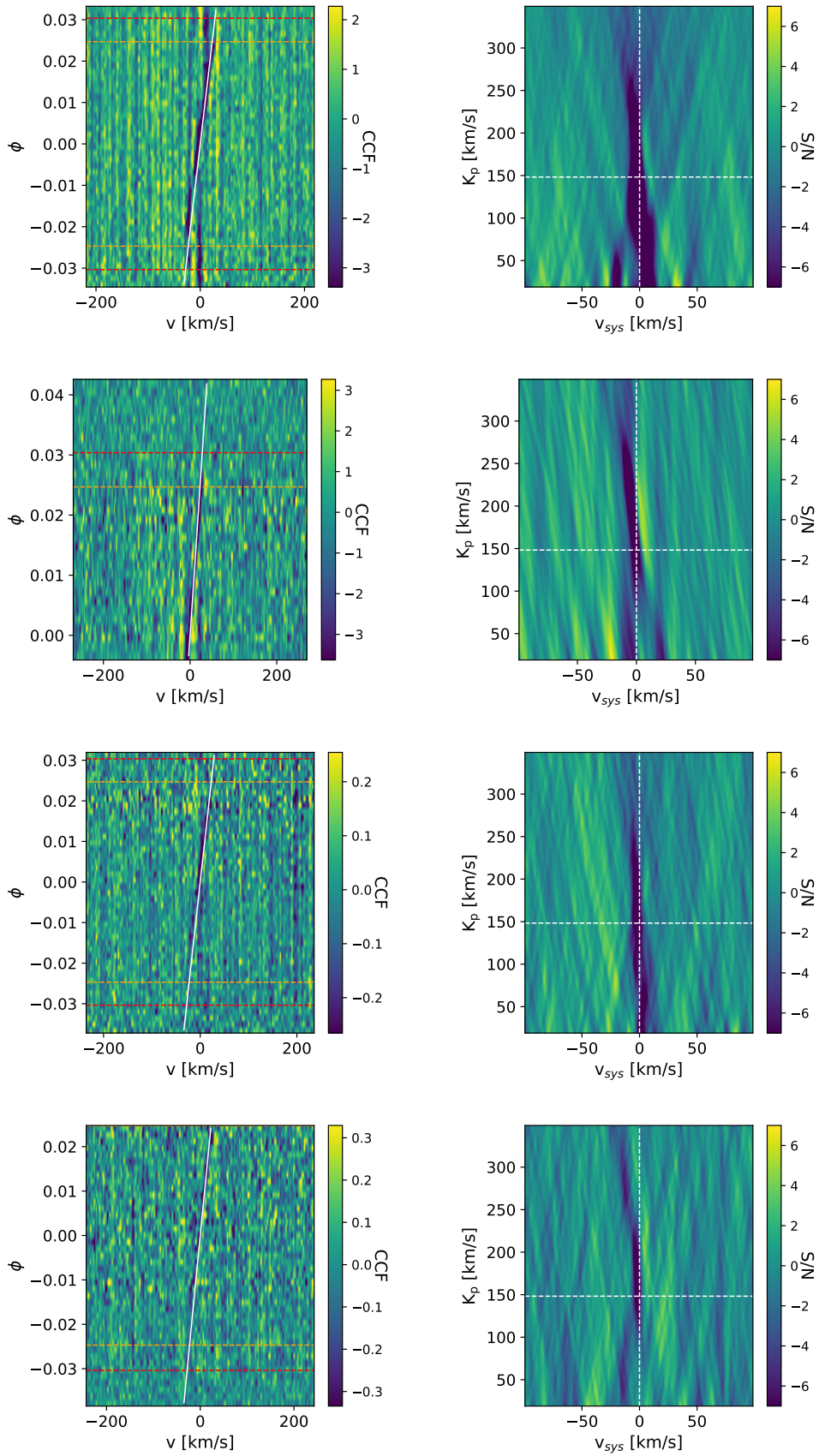


Fig. A.6: As Figure A.2 but for the VALD mask devoid of the Cr I, Fe I, Na I, and Ti I spectral lines.



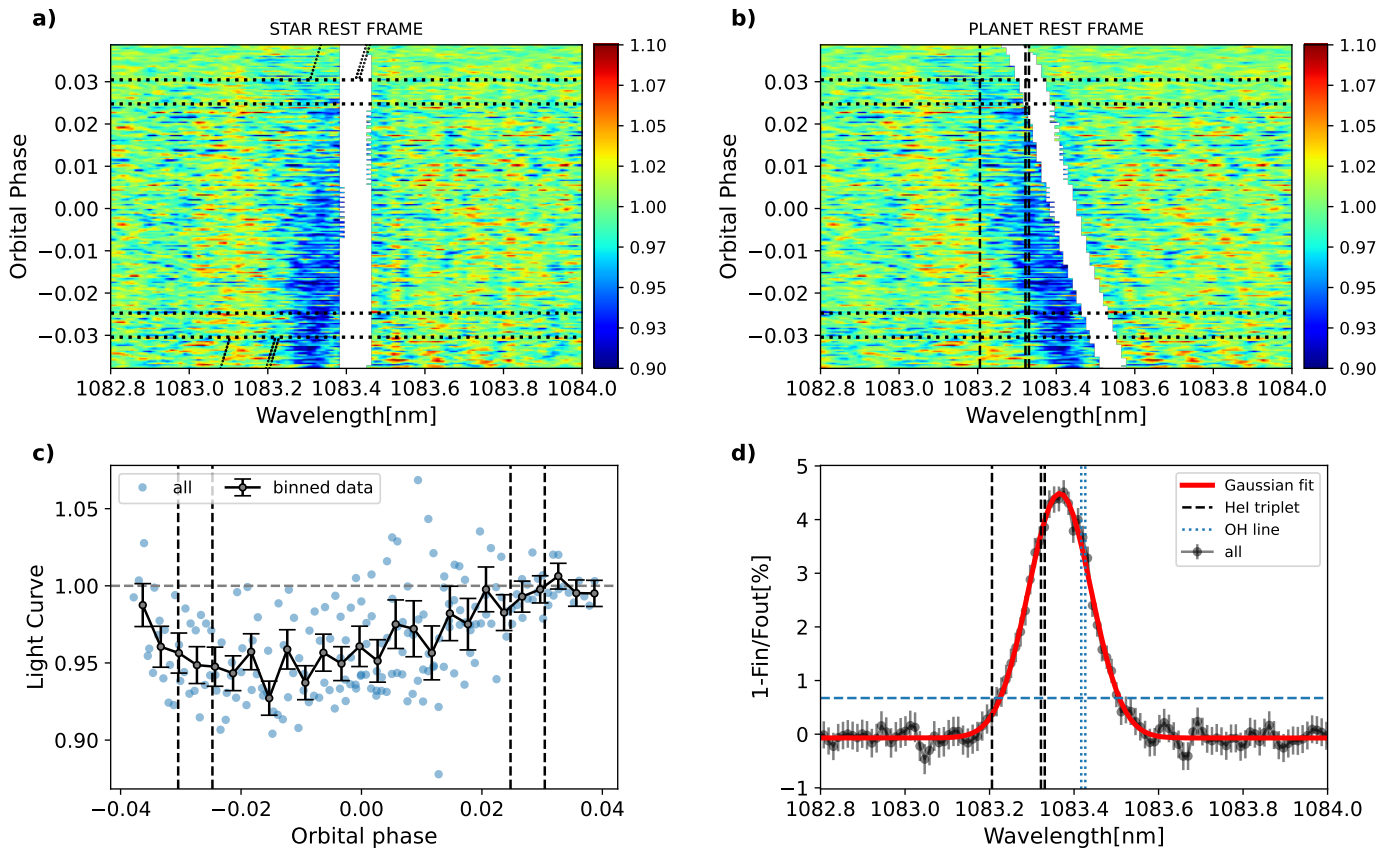


Fig. A.7: Same as Fig. 10, but considering all the available GIANO-B nights.

## HAT-P-67b

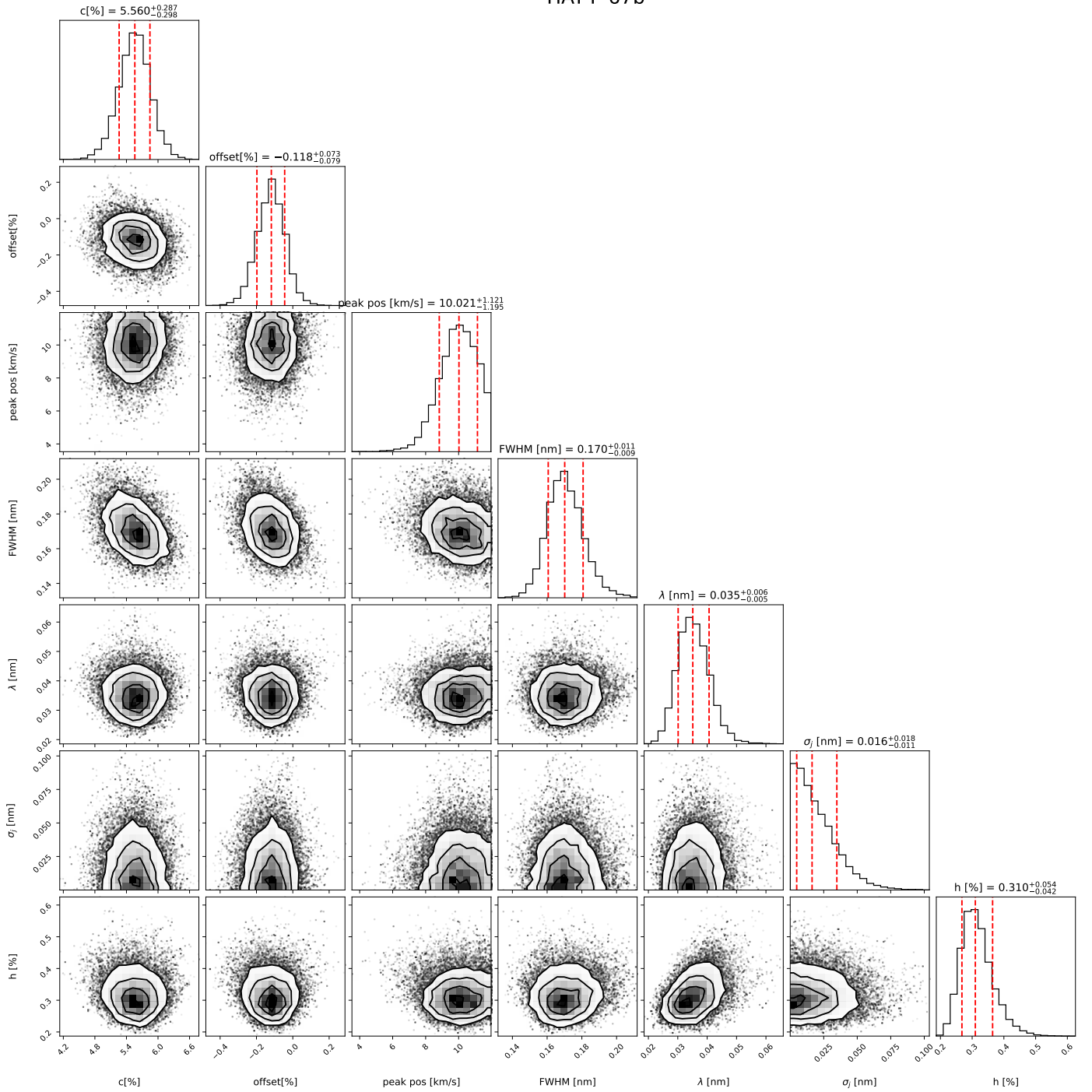


Fig. A.8: Posterior distribution of the investigated parameters in the DE-MCMC analysis of the He I triplet. The excess of absorption  $c$  [%], offset [%], peak position, and FWHM correspond to the parameters we used in the Gaussian fit, while the jitter term  $\sigma_j$ , the semi-amplitude of the correlated noise  $h$ , the correlation length  $\lambda$  were used to parametrize the SE kernel within the GP.

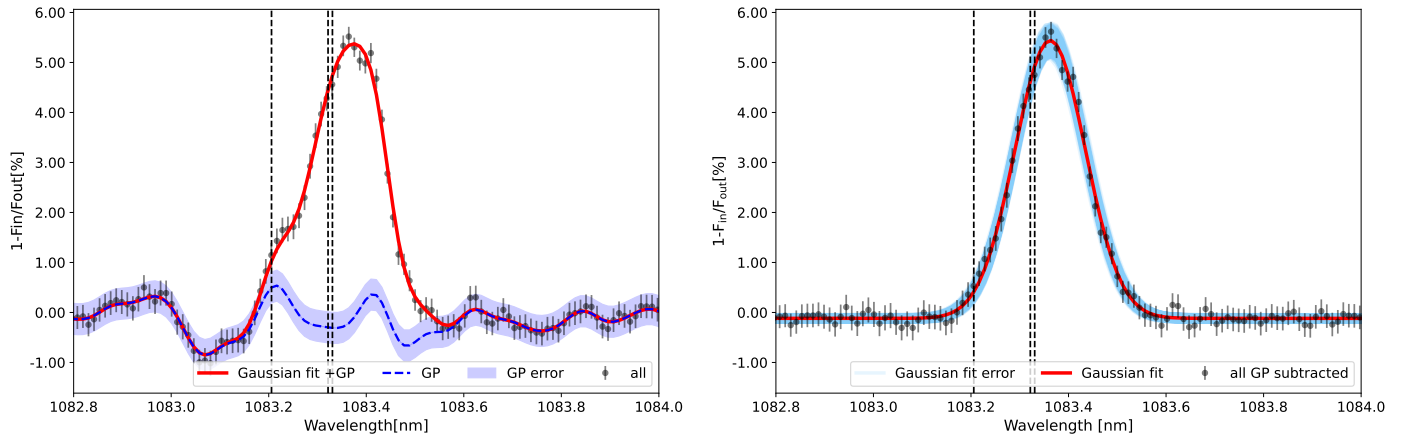


Fig. A.9: GP correction. Right panel: transmission spectrum centered on the He I triplet (in the planet rest frame) with overplotted the GP regression model, along with the  $1\sigma$  uncertainty intervals (in blue) and the Gaussian+GP model (in red). Left Panel: Final transmission spectrum after removing the GP model. The error intervals for the Gaussian fit were computed by displaying 1000 Gaussian fits within the  $1\sigma$  uncertainties of the derived parameters, spanning the 16%-84% quantiles. Vertical black dotted lines indicate the position of the He I triplet.

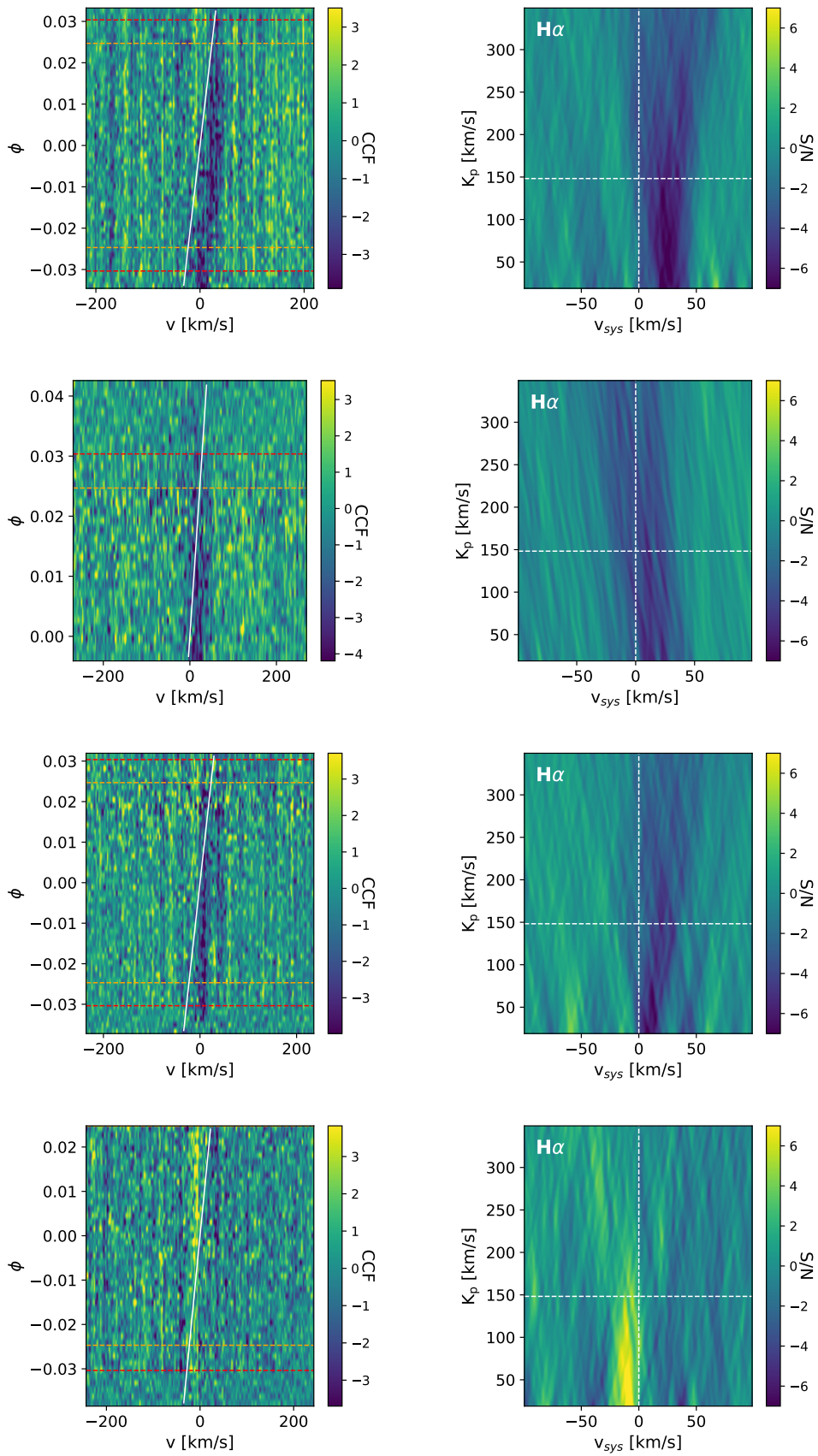


Fig. B.1: As Fig. A.2 but for a binary mask containing only the H $\alpha$  line.